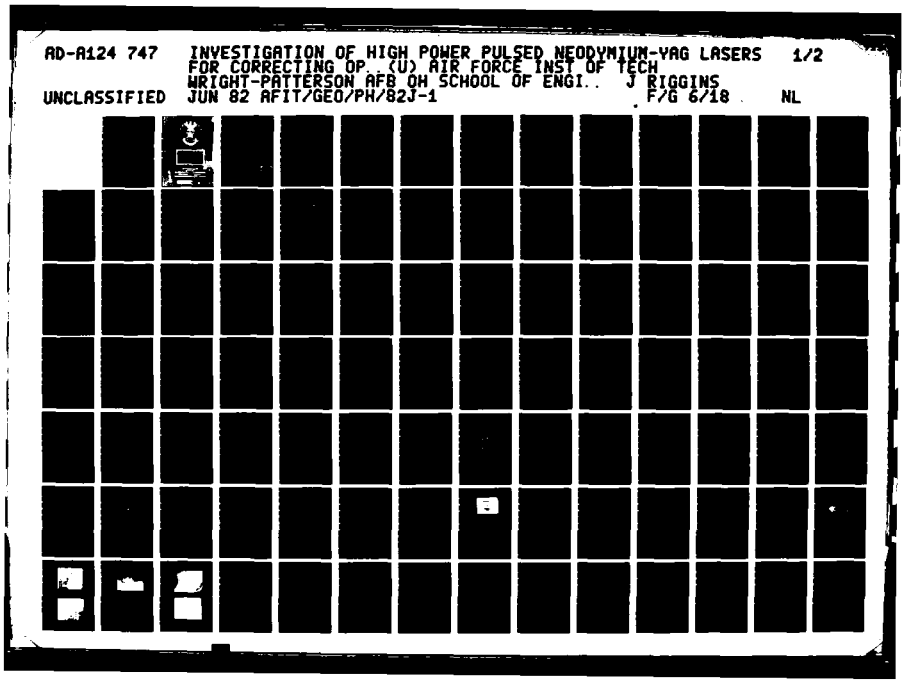
AD-A124 747 INVESTIGATION OF HIGH POWER PULSED NEODYMIUM-YAG LASERS 1/2
FOR CORRECTING OP..(U) AIR FORCE INST OF TECH
WRIGHT-PATTERSON AFB OH SCHOOL OF ENGI.. J RIGGINS
UNCLASSIFIED JUN 82 AFIT/GEO/PH/82J-1 F/G 6/18 NL

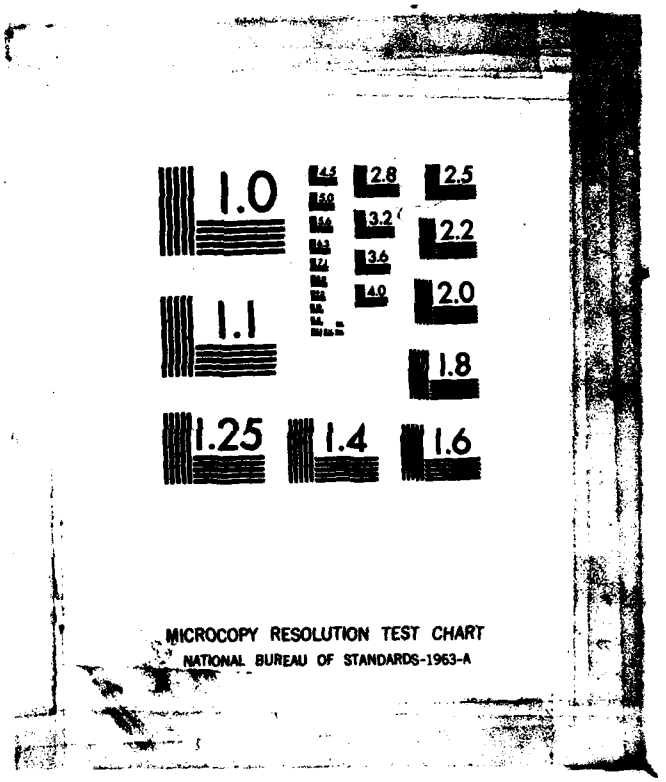
1.0
1.1
1.25
1.4
1.6
2.8
3.2
3.6
4.0
2.5
2.2
2.0
1.8
MICROCOPY RESOLUTION TEST CHART
NATIONAL BUREAU OF STANDARDS-1963-A

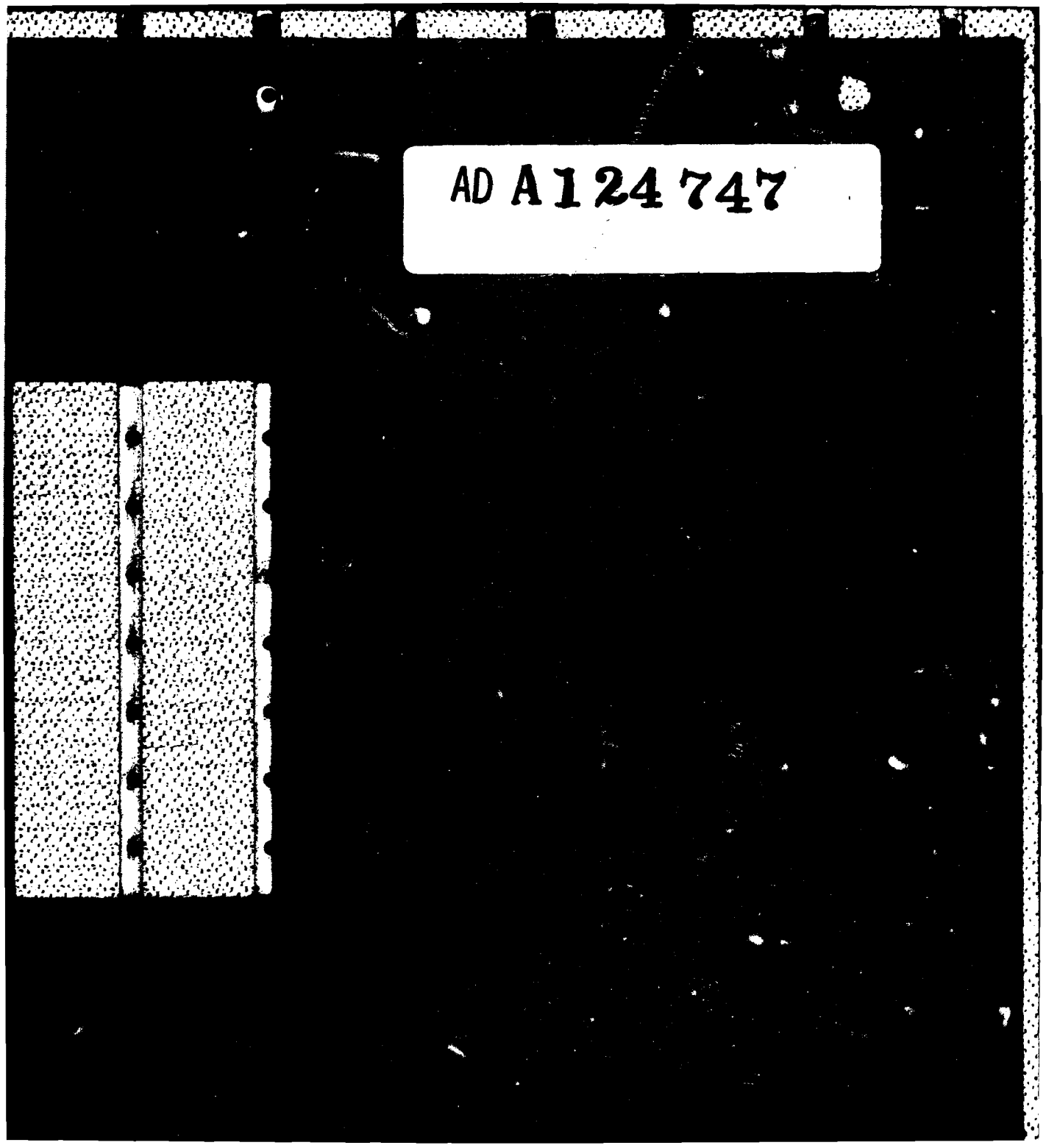

AFIT/GEO/PH/82J-1

INVESTIGATION OF HIGH POWER, PULSED, NEODYMIUM-YAG LASERS FOR CORRECTING OPACITIES OF THE HUMAN EYE
THESIS

James Riggins
AFIT/GEO/PH/82J-1 2Lt USAF

Approved for Public Release; Distribution Unlimited

AFIT/GEO/PH/82J-1

INVESTIGATION OF HIGH POWER, PULSED, NEODYMIUM-YAG LASERS FOR CORRECTING OPACITIES OF THE HUMAN EYE

Presented to the Faculty of the School of Engineering
of the Air Force Institute of Technology
Air University (ATC)
In Partial Fulfillment of the
Requirements for the Degree of
Master of Science

By

James Riggins, B.S.
2LT USAF
Graduate Electro-Optics

June 1982

Preface

This paper investigates some aspects of an exciting new laser application in ocular surgery--the opening of ocular opacities with the use of high power density laser pulses. The procedure could prevent thousands of post-cataract patients annually from undergoing risky surgery. The obvious direct benefits to other people served as the prime motivating factor in my choosing this topic.

This thesis could not have been completed without the help and support of many people.

I would like to extend a special thanks to Professor Leno S. Pedrotti, my thesis advisor, for his guidance and sincere personal interest.

I would also like to thank Ron Gabriel, George Gergal, and Russel Murray for their technical advice and assistance in the hardware construction.

Thanks must also be extended to Dr. Richard Keates, Jill McCune, and the rest of the staff at the Ohio State University Eye Clinic; and also to Roy McCord and Paul Goth of American Hospital Supply Corp. for their backing and technical advice.

Finally, and most importantly, I would like to thank my wife, Dawn, whose love and support (and, of course,

expert typing) made this project possible and prevented me from losing my sanity.

James Riggins

Table of Contents

List of Figures

LIST OF TABLES

List of Symbols

A	Optical Matrix Element
a	Spotsize Measuring Ribbon Width
B	Optical Matrix Element
BSS	Balanced Salt Solution
C	Optical Matrix
D	Optical Matrix Element, Beam Diameter
D_i	Cavity Mirror Diameter
d	Distance Behind Posterior Capsule
f	Focal Length
f#	F-number of Focusing Lens
g_i	Laser Cavity Parameter
h	Planck's Constant
I	Intensity
L	Reduced Laser Cavity Length
n	Index of Refraction
P	Power Incident on an Aperture
P_0	Power Transmitted Through an Aperture
RP	Reference Plane
R_i	Mirror Radius of Curvature
S	Standard Deviation for Error Analysis
t	Thickness of Cavity Mirrors
V_i	Compensated Ray Angle
v_i	Ray Angle
w_i	Gaussian Spotsize

w_{0i}	Gaussian Waist Spotsize
Y_i	Geometrical Ray Weight
z	Optical Axis
Z_{Ri}	Rayleigh Range
θ	Half Angle Beam Divergence
λ	Wavelength
ν	Frequency
Φ	Aberration Function

Abstract

A Q-switched Nd-YAG laser system with a 27ns pulse-width and focused spotsize diameter in air of 4.4μm is used in a series of experiments related to opening ocular opacifications. The maximum pulse energy is 10.89mJ yielding a peak focused intensity of 2.65×10^{12} W/cm^2.

Results of experiments designed to simulate opening an opacified posterior capsule after cataract surgery and glass IOL implantation indicate an occurrence of IOL shatter only when the IOL is in contact with the capsule.

Additional experiments on the optical breakdown characteristics of several fluids indicate balanced salt solution most closely models the breakdown characteristics of human vitreous.

A theoretical feasibility analysis of using the laser system to rupture vitreous strands concludes that only rupturing strands no farther than 4-6mm from the posterior capsule in an undilated eye can be safely attempted.

Finally, a general theoretical analysis on the effects of altering beam parameters--wavelength, pulsewidth, spotsize--reveals possible benefits of utilizing short wavelength (down to 500nm)/short pulsewidth systems (picosecond).

I. Introduction

Laser use in ophthalmology represents the earliest attempt at incorporating the laser in the field of medicine. A wide range of applications in eye surgery have been adopted utilizing the unique properties and capabilities of the laser. This thesis discusses and investigates a profoundly new application of the laser in ocular surgery.

Objective and Scope

This paper will investigate the use of high peak power, nanosecond laser pulses focused in the posterior chamber of the eye to rupture opacified posterior lens capsule tissue or vitreous strands through the creation of a spark plasma and associated shock wave. The author discusses current theories on the formation of the shock wave and its relation to laser beam parameters along with laboratory experiments designed to create and study shock waves and their effects in pig and human eyes. The experimental procedure will utilize a Q-switched Nd-YAG laser interfaced with an ophthalmic slitlamp to simulate the actual conditions under which the physician would perform the operation. The research will make no attempt, due to time and equipment limitations, to experimentally investigate the use of different laser wavelengths or pulse durations, nor will an attempt be made to design and build a complete surgical prototype to be used on human subjects.

The purpose of the experiment falls into two specific areas. First, because the posterior capsulotomy normally follows artificial intraocular lens (IOL) implant surgery, evaluating the effects of the laser pulses on implants of different materials and styles is crucial. Second, developing the ability to precisely focus the beam within the eye is necessary to reduce the risk of injury to healthy ocular tissue. This particular study will include a determination of the location of the spark plasma with respect to the focal point and an analysis of the predictability of the shape and size of the plasma. The final objective consists of a theoretical investigation of the use of other wavelengths, pulsewidths, and focused spot-sizes to optimize this surgical instrument.

Background

All ophthalmic uses of the laser in the past have been based on the thermal effects of the concentrated beam on the cells and tissue of the eye. For example the use of the ruby laser in retinal spot welding, the argon laser in photocoagulation and relieving pupillary block glaucoma (Ref 1:75), and recently, the CO_2 laser has been considered as a surgical knife for radial keratotomies (Ref 2) and performing corneal transplants.

In each of these surgical procedures, a particular wavelength of laser light is matched to the peak absorption characteristics of the area of interest in the eye and the beam is used to burn tissue. When using the laser to open

an opacified posterior capsule, the thermal effects are neither used nor desired.

A brief description of the physiology of the eye will aid the understanding of this operation. The iris, as shown in Figure 1 on page 4, separates the portion of the eye between the cornea and the lens into two sections, the anterior and posterior chambers. The posterior chamber ends at the 10μm thick tissue envelope containing the lens (the lens capsule), with the portion of the capsule facing the cornea being the anterior capsule and the portion facing the retina, the posterior capsule.

During a standard cataract operation, the opaque cataractous lens is removed and the loss of the lens compensated for by spectacles or contact lenses. Since 1949, however, more and more surgeons have adopted the delicate technique of artificial intraocular (IOL) lens implants to replace the original lens. At the present time, the most common form of implant surgery is the posterior chamber method, placing the artificial lens in the capsule left vacant by the removal of the human lens (Ref 3:271). The alternate method of implantation is one where the IOL is placed in the anterior chamber and either clipped to the iris (iris clip IOL) or held in place by protrusions into the posterior chamber (iridocapsular IOL) (Ref 4:58). One serious complication of unknown origin in the procedure manifests itself by opacification of the posterior capsule, causing a drastic reduction in sight.

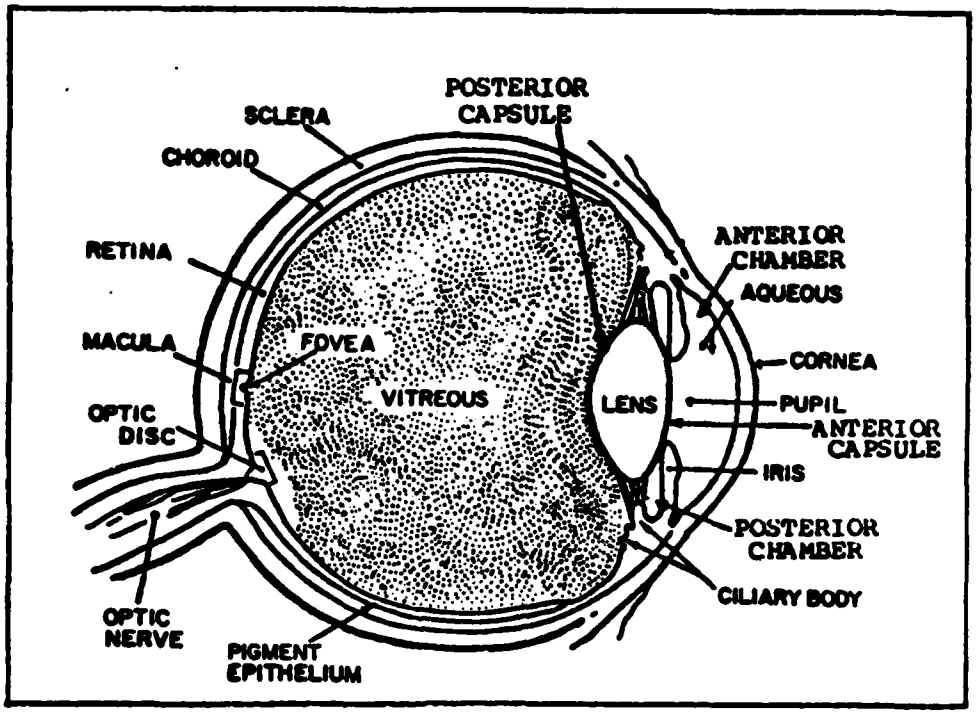

Figure 1. The Eye

Until recently, only additional surgery to open the capsule would remedy the unwanted opacification, with the exact form of surgery depending on the characteristics of the capsule. For a thin elastic capsule, a simple incision through the tissue, aided by the natural tension of the membrane, opens the capsule. However, for tougher or denser membranes the opposing action of two knives, the use of a vitrectomy tool, or the use of scissors may be required to cut out the capsule (Ref 4:56). Obviously, each procedure described above requires anesthetizing the patient and incising the eye, increasing both risk and recovery time, especially in elderly patients for whom implant surgery is most common.

These disadvantages point out the benefits of a laser system to open the capsule. Very simply, directing a laser beam through the cornea and pupil on the opaque membrane can be accomplished quickly, with no anesthetic, and with relatively little risk.

Aron-Rosa of France conducted an initial investigation in 1980 on human patients, using a laser system to open the posterior capsule after IOL implant surgery (Ref 5). Her system consists of a mode-locked Nd-YAG laser emitting 30 picosecond pulses modulated by a 1 hertz signal of 20 nanosecond pulsewidth. The energy per individual pulse at the entrance of the eye is 3 to 4.5 millijoules creating power densities from $1x10^{12}$ to $1.6x10^{12}$ Wcm^{-2} at the 50μm diameter focal spot.

Aron-Rosa and her colleagues operated on twenty post lens-implantation patients with opacified posterior capsules, using no anesthetic. With a series of five to ten laser shots focused on the capsule, the results were remarkable. In all cases the large power densities of the laser radiation opened the capsule but created no permanent intraocular pressure rise; no corneal, iris, vitreal, or retinal lesions; and only three patients developed a temporary anterior chamber reaction. Improvements in visual acuity ranged from the slight change of 20/30 to 20/20, to the large improvement of 4/200 to 20/20. Presently, Aron-Rosa performs this procedure daily on a number of patients with no indications of deleterious effects.

Fankhauser, van der Zypen and associates in Germany describe the use of a similar system to treat various disorders in the anterior portion of the eye. Although they made no attempt to open the posterior capsule, the mechanism operating on ocular tissue--in this case the iris--is the same, and their results enhance the knowledge of the effects of high power pulses in the eye.

The Fankhauser system consists of a Nd-YAG Q-switched laser producing 12ns pulses of 200mJ peak energy. The laser beam focuses to a 50μm diameter spot providing a peak energy density of $7x10^{11}$ to $8x10^{11}$ Wcm^{-2}. Compared to the Aron-Rosa experiments, the Fankhauser system uses longer pulses and greater energy per pulse to maintain a comparable power density within an identical spot.

Van der Zypen and Fankhauser successfully treated acute and chronic angle-block glaucoma and pupillary-block glaucoma but were unsuccessful at treating chronic simple glaucoma and pigmentary glaucoma. They were also successful at opening a number of pupillary membranes of various elasticities and pigmentations, a procedure similar to opening the posterior capsule (Ref 6).

At this point, Dr. Richard Keates of the Ohio State University Ophthalmology Clinic, who had studied the work of the European ophthalmologists, requested that the Air Force Institute of Technology conduct a feasibility study of a Q-switched laser system for opening the opacified posterior capsule as an alternative to the cost prohibitive

mode-locked system of Aron-Rosa. If successful, this laser system would benefit many more than the hundreds of post capsulotomy patients Dr. Keates alone presently treats with complicated surgery. In addition, Dr. Keates desired a study of the feasibility of applying the system to breaking vitreous strands, a condition consisting of cellular strands in the vitreous humor, generally caused by disease or trauma to the eye.

A knowledge of the optimal system design and of the definitive measurements to be made, requires an understanding of mechanisms operating within the ocular tissue when coupled with high peak power, short pulse energy. Chapter II addresses this matter in detail.

II. Biological Theory

Introduction

Various physical, chemical and biological processes occur when laser light interacts with ocular tissue, the type and extent of which depend on a multitude of factors. These factors include beam parameters--size, frequency, pulsewidth, power density, and polarization; and tissue parameters--chemical composition, optical properties, etc. Owing to the interrelated nature of many of these parameters, determining or predicting their precise effects on differing types of ocular tissue is difficult and has led to much controversy, both among physicists and ophthalmologists. This chapter provides an attempt at correlating current medical and scientific theories and observations to provide an understanding of the basic phenomena associated with coupling laser radiation and human tissue.

Effects of Laser Radiation on Ocular Tissue

Thermal, photochemical, and mechanical effects result from laser energy deposited in the eye. Although only mechanical effects are desired and needed to open opacified tissue, the other two pose potential side effects and must be understood when designing the laser system.

Thermal Effects

Thermal effects are the best understood and studied of the laser effects in the eye. They occur primarily in the pigmented tissue of the eye such as the iris and retina

where large absorption coefficients for visible and near infrared wavelengths or greater exist, and when irradiating with relatively "long" pulsewidths. The effects, stemming from molecular vibrational excitations, mainly manifest themselves as burning and lesion formation.

Van der Zypen, Fankhauser and associates, after extensive study of laser radiation on the iris, theorize that heat conduction, local evaporation, and fluid circulation control the thermal effects in ocular tissue. They argue that the tissue temperature of the iris may not rise above the boiling point because the onset of local evaporation initiates fluid circulation in the anterior chamber which, along with thermal conduction, acts as a cooling and temperature limiting mechanism. If, however, thermal conduction is disrupted by a vapor layer between the irradiated tissue and surrounding tissue, then local temperatures could be expected to exceed the boiling point. Experimental measurements with a CW argon laser of 0.75W focused to a spot of 30-100μm diameter, agree closely with the theoretical values predicted when using the heat conduction properties of water as a model (Ref 7:88-90).

The damage created by the argon laser on the iris consists of crater formation in the tissue with varying degrees of cellular damage in the surrounding area out to approximately 200μm from the rim of the crater (Ref 7:82-83).

Other than cellular destruction, heating of the eye is believed to cause opacities in the cornea and lens. This

damage occurs either through direct heating of the cornea by far infrared light such as CO_2 laser radiation, or by indirect heating through thermal conduction from an irradiated iris or retina (Ref 8:144).

Photochemical Effects

A less well understood damage mechanism of ocular tissue is that due to photochemical effects, usually associated with blue and ultraviolet laser light. The basic principle associated with the photochemical process involves light where the quantum energy of a single photon breaks the molecular bonds of the tissue or cells and creates biochemical reactions (Ref 9:1269).

Photochemical damage to the retina manifests itself as a lesion. Damage to the cornea, where UV effects are most common due to strong absorption in the UV, includes keratoconjunctivitis and photokeratitis. Both of these are painful conditions which last two to three days after exposure and are caused by damage or destruction of the corneal epithelial cells. Higher doses of UV radiation may cause damage beneath the epithelial layer opacifying the cornea, and requiring a corneal graft (Ref 8:108-110).

Photochemical damage to the lens manifests itself as a degradation of lens constituents, causing long term or permanent opacifications (cataracts) due to an extremely slow rate of cellular repair. Although large doses of radiation may cause an obvious photochemical reaction in a matter of hours or days, it has been shown that with

slightly lower doses years may pass before photochemical damage to the lens appears (Ref 8:106, 112-114).

With ocular tissue containing melanin pigment, such as the iris, photochemical damage might also include melanoma (cancer of the melanin containing tissue); however, the data on this theory is inconclusive and strong concentrations of melanin may actually inhibit the formation of melanoma (Ref 8:116).

Mechanical Effects

Mechanical damage to the eye, as a result of acoustical waves or hydrostatic shock waves, is a subject of controversy. While few deny its existence, wide spread agreement on extent of damage and formation is still lacking.

Basically there exist two sources of mechanical damage. The first, the acoustical wave, is the result of the absorption of a large quantity of energy in a short period of time, creating a phase change and rapid expansion of the tissue. The second source, and the basis of the surgical procedure reported in this paper, is the hydrostatic shock wave, created as the result of spark plasma formation in the tissue. Subsequent sections describe the current theories on the formation of both spark plasma and shock wave in detail.

Extensive research by van der Zypen, Fankhauser, and associates on shock and acoustical wave damage in iris tissue, indicate damage can be expected over a much larger area than would be seen with thermal damage. Shock wave

formation in the iris can create diffuse hemorrhaging, tearing and fragmentation of cells, and the ejection of blood corpuscles well into surrounding tissue (Ref 7:135-136). Similar damage, with more severe consequences, is effected by this mechanism on the retina, where large scale damage to photoreceptors can lead to partial or total blindness.

The above overview of laser radiation effects on ocular tissue makes one aware of the potential undesired effects which may accompany the use of high power lasers in clearing opacifications of the eye. It is necessary now to understand the correlation of the three damage mechanisms with the laser beam parameters. The understanding will be an aid in optimizing the parameters for the design of the surgical tool while minimizing dangerous side effects.

Correlation to Frequency

The frequency of the incident laser radiation is critical in two respects. First, the frequency, or more specifically the energy of individual photons, determines which of thermal or photochemical mechanisms, or combinations thereof, will prevail in the tissue. Second, the extent of the damage due to each mechanism relates to the absorption coefficient of the particular tissue which may be strongly frequency dependant.

The optical frequency where thermal mechanisms end and photochemical mechanisms begin is not a distinct one. Lerman creates the theoretical divisions at 1.6eV photon energy and below for thermal damage; 1.6eV (λ=776nm) to

12.4eV (λ=100nm) photon energy for photochemical damage; and 12.4eV to 1.24×10^{8}eV photon energy for ionization where the quantum energy exceeds the binding energy of the electrons (Ref 10:215).

Experimentation on retinas of monkeys by Ham and associates created retinal lesions due only to photochemical mechanisms with He-Cd wavelengths of 441.6 to 514.5nm, lesions due only to thermal mechanisms with a Nd-YAG wavelength of 1.064μm, but lesions due to a combination of the two mechanisms with intermediate wavelengths of 580nm to 632.8nm, thus demonstrating the frequency dependence of the damage mechanism (Ref 10:217-18).

Similarly, the "action spectrum" (the relative level of photochemical response vs wavelength) of photokeratitis in the cornea was shown by Cogan and Kinsey to be confined in the ultraviolet region between 210nm and 320nm (Ref 10:126-26).

The frequency dependence of absorption coefficients for the various portions of the eye establishes the second important aspect of the laser beam frequency. The importance of frequency dependence cannot be understated in surgical applications such as the one being examined in this paper. Here we require that high energy densities be focused in a small volume while doing no damage to other segments of the eye in the path of the beam; therefore, a good working knowledge of the absorption characteristics of the eye is crucial.

Table I on page 15 indirectly illustrates the relative absorption of the cornea, the aqueous humor, the lens, and the vitreous humor, by indicating the percent of radiation initially incident on the cornea which successively reaches the segments deeper in the eye (the value at the cornea always being 100%).

Two values for each segment are provided, "direct" and "total". The "direct" figure is the percentage due to direct transmittance while the "total" figure accounts for both direct transmittance and forward scattered radiation (Ref 11). Because the values of Table I ultimately yield only the percentage of radiation reaching the retina, one other important set of data should be presented: Figure 2 below indicates the absorption in the retina and choroid as a function of wavelength (Ref 12:19). The importance of the data in Table I and Figure 2 will become evident during the discussion of the design theory.

Correlation to Pulsewidth

Like frequency, the pulsewidth is a highly significant parameter in determining the type and extent of damage from laser radiation in the eye.

When utilizing the band of laser radiation which can elicit a thermal response in the eye (i.e. the infrared through most of the visible), the effect of pulsewidth is one of determining whether the primary damage mechanism will be thermal or mechanical.

It is widely accepted that mechanical effects are

TABLE I

Percentage of Radiation Incident on Cornea Which Reaches Successive Segments of the Eye

Wavelength (nm)	Aqueous		Lens		Vitreous		Retina	
	Direct	Total	Direct	Total	Direct	Total	Direct	Total
260								
280	0.1	0.1	0.0	0.0				
300	2.0	8.3	1.4	0.0	0.0	0.0	0.0	0.0
320	26.3	55.5	19.3	40.7	1.3	3.7	0.8	2.7
340	34.1	63.3	26.6	49.3	0.5	1.0	0.3	0.8
360	39.0	66.2	31.8	54.0	0.1	0.3	0.1	0.2
380	42.3	67.7	35.7	57.2	0.4	0.9	0.3	0.7
400	44.8	62.3	38.5	53.6	4.8	7.5	3.0	5.9
420	44.8	61.3	39.4	53.9	22.1	34.5	12.4	27.6
440	52.1	75.0	46.6	67.1	33.1	60.3	23.8	56.1
460	56.0	83.3	50.9	75.8	37.7	70.5	28.4	67.0
480	58.9	85.7	54.5	79.2	41.4	74.1	31.6	71.5
500	60.8	87.2	57.2	82.0	44.6	77.1	34.6	74.0
550	64.3	89.6	61.7	86.0	44.4	81.7	34.4	78.5
600	69.2	90.6	66.4	87.0	56.8	82.7	45.4	80.2
650	71.1	91.5	67.9	87.4	59.1	83.9	47.6	81.4
700	73.5	90.6	69.8	86.0	61.4	82.6	49.7	80.1
750	75.5	91.1	71.7	86.5	63.4	83.0	51.7	77.6
800	76.9	91.5	72.7	86.4	64.7	82.9	52.3	77.5
850	78.4	92.5	74.1	87.4	66.3	83.8	52.0	76.3
900	79.4	92.5	74.7	87.0	66.8	83.1	50.3	73.1
950	78.9	92.5	68.6	80.5	58.3	72.5	35.0	47.8
1000	79.4	91.5	63.5	73.2	51.4	61.5	22.9	34.4
1100	82.8	92.1	70.8	78.8	60.8	69.3	39.5	50.6
1200	77.9	89.0	47.1	53.8	30.2	36.0	3.8	7.2
1300	79.8	87.7	49.8	54.8	33.4	38.4	4.2	6.0
1400	38.9	57.4	0.2	0.3	0.0	0.0	0.0	0.0
1500	26.8	32.1	0.0	0.0	0.0	0.0		
1600	56.5	66.2	4.9	5.8	0.5	0.8		
1700	61.8	69.2	9.3	10.4	1.1	1.6		
1800	53.5	59.9	2.7	3.0	0.1	0.2		
1900	2.9	4.9	0.0	0.0	0.0	0.0		
2000	1.0	2.9	0.0	0.0				
2100	16.6	21.4	0.0	0.0				
2200	25.8	30.2	0.1	0.1				
2300	17.5	20.4	0.0	0.0				
2400	5.4	7.8						
2500	0.0	0.5						

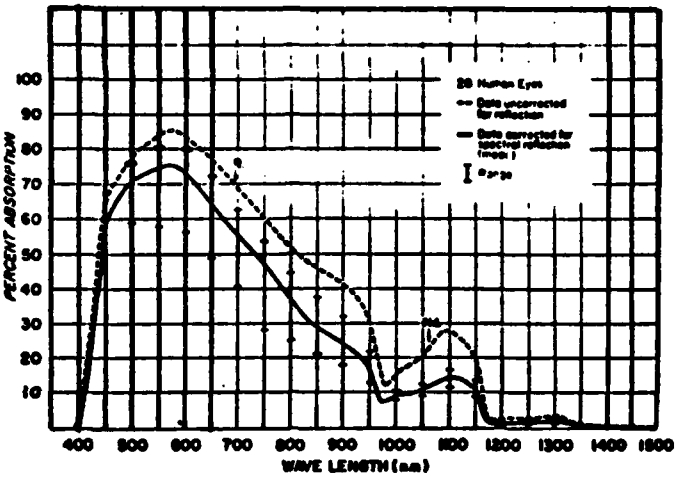

Figure 2. Percent Absorption in the Retina and Choroid (Ref 12:19)

present when pulsewidths are on the order of nanoseconds or shorter. Nevertheless, it is interesting that the same conclusion was reached by different groups with contradictory data. Sliney and Wolbarsht determined that energy density threshold for retinal lesions increased as the pulsewidth decreased from 1μs to 20ns, concluding that the energy must be dissipated through nonthermal mechanisms (Ref 8:130). Ham and co-workers, on the other hand, measured a decrease in energy density threshold for retinal lesions and concluded the damage must not be strictly thermal (Ref 13:176).

A precise pulsewidth, where the transition between thermal and mechanical effects occurs, obviously does not exist; however, recent work on laser effects in the iris demonstrated that even in pigmented tissue, pulsewidths as

short as 1ms and with pulse energies up to 2.3J, the damage produced was due solely to thermal means; no shock or acoustical waves were produced. Damage was, though, less extensive than with CW radiation of less energy. This was attributed to the process of convective energy transport which distributes the heat over a large volume, a factor often neglected in many heat conduction models (Ref 7:115-16). When pulsewidths are reduced to the nanosecond region and shorter, the time is too short for the energy to be dissipated thermally, and damage near the focus of the beam may be attributed almost exclusively to mechanical damage.

In the case of irradiation of pigmented or highly absorbing tissue at the wavelength of interest, rapid phase change or vaporization result in the production of acoustic waves. Cleary theorized and experimentally verified to some degree that acoustic transients are generated both above and below the threshold for vaporization. Above the threshold, the rapid growth of a vapor cavity generates the acoustic wave while also generating severe localized damage. Below the threshold, acoustic transients will be produced from the thermal expansion of the tissue. In both cases, the pressure amplitude will be inversely proportional to the square of the radius of the wave, and therefore the waves are rapidly attenuated and damage is confined to a small area when the beam is focused to a small spot (Ref 13:180-184, 193).

In the case of irradiation of either pigmented or transparent tissue or fluid, mechanical damage can be created by exceeding the power density threshold for optical breakdown, causing a spark plasma and associated shock wave. The formation of the shock wave and plasma is dependent on a short pulsewidth by enabling large power densities to be achieved with minimal energy losses through thermal dissipation.

The formation of the spark plasma in pigmented tissue would lead to the existence of many of the damage effects described to this point. The extreme temperatures near the beam axis at the focus causes severe localized thermal damage while the mechanical waves produced will be a combination of the breakdown shock wave and the vaporization acoustic transients described by Cleary, with the precise damage attributed to each made difficult to separate (Ref 7:142-43).

The formation of optical breakdown and the associated shock wave in a transparent medium, such as the human vitreous, forms the basis of the surgical procedure described in this paper and a summary of the theories on its formation is presented in Chapter III.

Correlation to Power and Energy Density

The correlation of laser effects in ocular tissue to power density of the incident laser beam is useful when discussing the threshold for optical breakdown in various types of tissue. The extent of photochemical damage, by

its very nature, is a function of energy density as opposed to power density (Ref 8:108). On the other hand, the extent of thermal and acoustical wave damage involves both parameters; with "long" pulsewidths, the energy density determines the extent of thermal damage while with "short" pulsewidths, the energy density determines the existence and size of a vapor cavity, and hence, the amplitude of the acoustical wave.

As can be seen, the description of the correlation of laser beam parameters to power and energy density illustrates the interdependence of all parameters described thus far. It is important at this point to reemphasize that the correlations of the various beam parameters to the damage mechanisms have been described *in* very general terms, with the emphasis being placed on experimental data rather than on theoretical models. Although laser beam effects in the eye have been studied since the earliest lasers were developed, much controversy over effects due to the complex biological nature of the eye still exists on the subject, thereby rendering experimental results still more "acceptable" than the predictions of theoretical models.

III. Plasma Theory

Introduction

At the foundation of this project lies the theory on dielectric breakdown, plasma, and shock wave formation since it is the shock wave which ultimately breaks the opacified posterior capsule and vitreous strands.

The literature on plasma theory is voluminous and ranges from the highly theoretical to the strictly observational. The majority of early plasma research was performed with gases while recently the emphasis has shifted to solids and dielectric coatings. The literature on dielectric breakdown in fluids, especially water, is sparse and data on ocular fluids is nonexistent. Therefore, the theory presented in this chapter will consist of a cautious extension of theory and experimental results in gases and solids to fluids--only where it is felt that the extensions are reasonable, and only with the understanding that the speculation will be tested experimentally in this or future projects. Rigorous plasma physics theory will be avoided. Instead this discussion will concentrate on general theory and experimental observations with the simple goal of understanding plasma formation in the eye and predicting the benefits of altering the beam parameters.

This chapter is divided into four section, each describing one of the basic stages of dielectric breakdown

in transparent media: initiation, ionization, absorption, and shock wave formation.

Initiation

The initiation process is of critical importance. The surgeon must be assured of plasma formation on every laser shot into the eye to avoid irradiating the eye more than is necessary.

The initiation stage for one type of ionization, cascade ionization (described in the next subsection), involves the formation of the initial free electrons to begin the cascade process. The free electron formation is caused by thermal heating of contaminant particles or by multiphoton absorption in an impurity. Thermally generated electrons are generally associated with relatively long pulses (>20ns), and long wavelengths (>3μm). At short pulsewidths and wavelengths (t_p<200ps and, λ<690nm), the probability of multiphoton absorption initiation becomes high and may dominate (Ref 14:351). It becomes clear why this is so when one understands the process of multiphoton absorption. Normally, the absorption of a photon will take place only if an excited energy state corresponding to the quantum energy of the photon, ($h\nu$), exists. However, in a time less than $1/\nu$, a virtual state with energy $h\nu$ may exist, allowing absorption of a photon which otherwise would not be absorbed. Successive application of this theory shows that a $2h\nu$ state can be reached if two photons are absorbed in a time less than $1/(2\nu)$, and so on. In

this manner an energy of ionizing magnitude may be absorbed (Ref 15:626-627). Note that the higher the quantum energy of the incident photons (shorter wavelengths) the fewer the photons which need to be absorbed to cause ionization; but the greater the required energy flux due to the decreased virtual state lifetime.

The conclusion that initial electrons, and hence initiation of breakdown, is dependent on impurity concentration is of profound significance in this project, for it affects directly the pinpointing of the location of plasma formation in the eye. This generally accepted conclusion has a basis in a large number of plasma investigations. David Milam describes laser initiated breakdown in argon gas at 20 and 500psi with a ruby laser. At the lower pressure, where direct multiphoton ionization is theoretically the dominant ionization mechanism, a distinct breakdown threshold existed. However, in high pressure argon, where a cascade ionization process initiated with electrons from either multiphoton absorption or thermal generation is predicted, a statistical nature of breakdown occurrence existed, attributed to the probability of finding an absorbing impurity in the focal volume (Ref 14:350-51). Note here the important distinction between complete ionization through multiphoton absorption, and creating only seed electrons for cascade ionization through multiphoton absorption.

Boni and Meskan, going one step further, used 30ns, Nd-YAG pulses (λ=1.06μm) and demonstrated an order of magnitude difference in breakdown of air between filtered air (0.1μm filter) and air containing 68μm carbon particles (Ref 16:115). The same statistical nature has also been observed with ruby laser irradiation in alkali-halide solids (Ref 17:379). Milam extends his discussion of statistics in gas breakdown to observations on the "explosive" thresholds in solids where arbitrarily small breakdown damage areas cannot be created. He contends that the explosive threshold at longer pulse times, is due to the absence of an absorbing impurity in the focal volume. Hence, when the laser power is increased, extending the high irradiance volume, much more than enough energy exists to sustain ionization. By reducing the pulse times to appropriately short intervals, mulitphoton absorption dominates as the total ionizing mechanism. The seed electrons from impurities are then no longer important and the explosive thresholds disappear (Ref 14:352).

The statistics described above lead quite naturally to a dependence of initiation process on focused spotsize, under conditions where cascade ionization is expected. Indeed, experimental results have indicated a threshold increase for ionization with decreasing spotsize, which most investigators attribute to the decreased probability of finding an impurity atom in the focal volume. For the sake of completeness, other theories on breakdown and

threshold dependence include a) resonant radiation whereby excited atoms lose energy through spontaneous emission; which for large focal volumes could be reabsorbed, thus lowering the threshold; b) self-focusing; and c) stimulated Raman scattering losses (Ref 18:53).

A critical aspect of breakdown initiation and one which is often overlooked or dismissed as negligible is the effect of primary spherical aberration of the focusing optics.

In the attempt to produce higher flux densities by focusing to smaller and smaller spotsizes, the f-number (f#) of the system (defined here as the ratio of the diameter of the beam incident on the lens to the focal length of the lens) is often reduced to the point where primary spherical longitudinal aberration increases the focal volume dramatically. This inevitably leads to inaccurate interpretations of breakdown threshold intensities and may possibly be a factor in the production of multiple collinear spark plasmas which are reported in many investigations. Just how sensitive the shape of the focal volume is to spherical aberration was demonstrated by Aron, Ireland, and Morgan who analytically solved the Fresnel-Kirchhoff intensity integral written as a function of primary spherical longitudinal aberration. The calculation assumed a plane wave incident on the lens. As an example of their results, Figure 3 on page 25 illustrates the theoretical intensity profiles along the optical axis

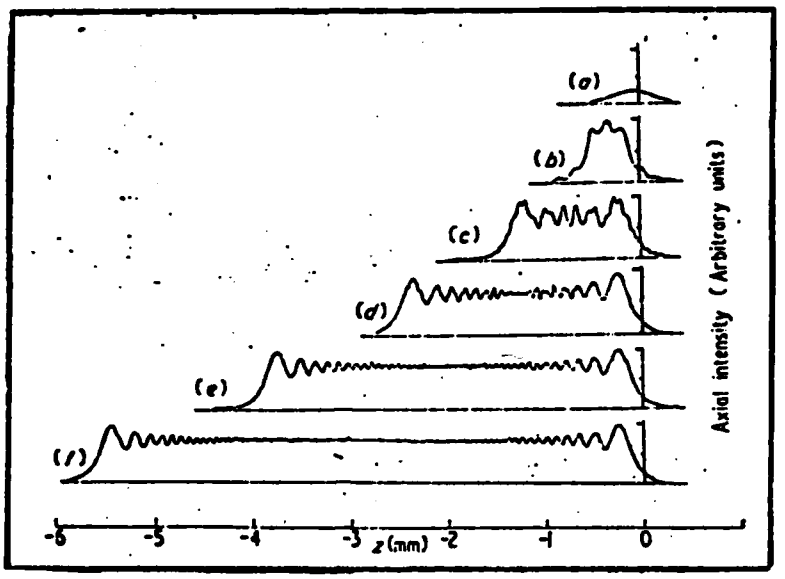

Figure 3. Effects of Spherical Aberration on Focal Volume. A lens with an f=2.5cm focal length is used in the calculation for which the beam diameter and aberration function are (a) 0.3cm, 0.13λ; (b) 0.6cm, 2.0λ; (c) 0.9cm, 10.5λ; (d) 1.2cm, 32.5λ; (e) 1.5cm, 80λ and (f) 1.8cm, 164λ. Gaussian beam waist is located at z=0 (Ref 19:1909).

for λ=1.06μm, the focal length f=2.5cm and the input beam diameter, D, varied to yield a range of aberration function values for the fixed lens shape of 0.13λ to 164λ (Ref 19:1908-09).

An intriguing aspect of these intensity profiles--which bear directly on the discussion of the plasma characteristics in the next chapter--is the lack of symmetry around z=0 (the Gaussian beam waist) for the aberrated systems. The implication is that when the laser intensity has been increased to achieve a breakdown threshold density near the focus, there now exists a virtually constant probability of forming a breakdown up to several millimeters upstream of the focus. For this particular example, that region amounts to many hundreds of Rayleigh ranges (957, for example, using Figure 3(d)). The Rayleigh range is used as

an indication of the length of the focal region. It is defined as the distance from the waist or focus of a Gaussian beam, along the optical axis to the point where the beam radius has increased to $\sqrt{2}$ times its value at the waist (see Figure 4). Aaron and associates also performed an analysis of where the use of the Gaussian beam equations fail with respect to increasing aberration function and determined the validity of the equations if the aberration function is kept less than 1λ (Ref 19:1913).

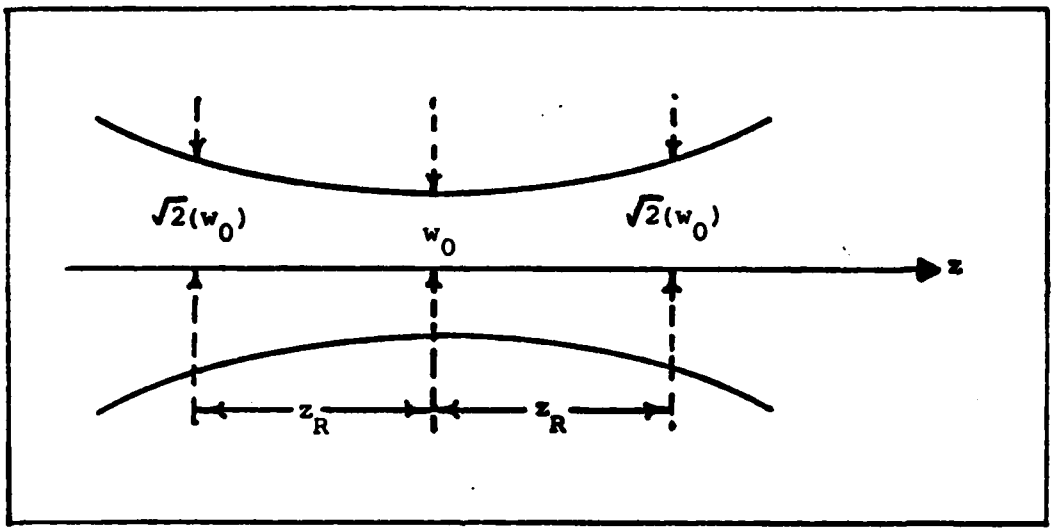

Figure 4. Illustration of Rayleigh Range

Ionization

As stated in the last subsection, physicists generally accept the existence of two modes of ionization: cascade ionization and ionization through multiphoton absorption.

In cascade ionization the initial "priming" free electron gains energy through "inverse bremsstrahlung" absorption. In this process, the electron absorbs light

quanta of the incident beam in the presence of an atom until sufficient energy has been reached to cause an ionizing collision with an atom. At this point, then, two free electrons of low energy exist and the process repeats itself, forming the "avalanche" ionization (Ref 20:625-26; 21:338). In gases of low pressure, however, and with the use of short pulsewidths (<1ns), cascade ionization will not have time to form and the dominant ionization mechanism becomes multiphoton absorption. However, if one maintains short pulsewidths but now irradiates solids or liquids instead of gases, the transition from cascade to multiphoton ionization is not as clear. Bloemberger theorizes that cascade ionization is the dominant mechanisms in crystalline solids when irradiating with near and far infrared wavelengths and pulsewidths as short as picoseconds. He believes, however, that cascade ionization loses its dominance with either higher frequency light or subpicosecond pulses (Ref 17:382). It should be pointed out that, at the present time, lasers with subpicosecond pulses are not yet available. However, there are many lasers operating with high frequency emission.

Varying a third parameter, spotsize, also affects the dominance of cascade ionization. The dependence is based on free electron diffusion drift, whereby with small focal volumes and especially in gases, electron diffusion out of the focal volume may be sufficient to inhibit cascade ionization at intensities near threshold (Ref 20:657).

Although this mechanism may operate in gases, most dismiss its importance in solids and at pulsewidths less than 10^{-8} sec (Ref 17:381). This author attaches a minimal importance to this mechanism in liquids where molecule densities are very high compared to gases.

A final mechanism operating on threshold levels after preionization may be that of self-focusing; however, the exact effect, if any, is extensively debated and unclear, and will not be described in this paper.

Absorption

Knowledge of the spatial propagation of the plasma after the onset of breakdown becomes critical in the design and use of the surgical tool. The beam must be focused in the eye such that migration of the plasma will not cause damage to healthy tissue.

In both gases and solids, observation of the primary plasma (the plasma forming in the region of highest intensity) indicates that it is pear shaped, with the wide bulb propagating upstream toward the focusing lens. This shape is believed to be caused by rapid absorption and heating at the leading edge of the plasma which serves as a preionization mechanism for the remaining incident light (Ref 21:3817).

Measurements of plasma absorption have shown that 50 to 90% of the beam is absorbed or scattered in the breakdown process. With nanosecond pulses and intensities somewhat above threshold, the probability of plasma formation down-

stream of the initial plasma becomes high. This is due to the plasma expanding with time and becoming more and more transparent to the incident radiation which can then create a breakdown beyond the initial plasma (Ref 18:74). Plasma absorption and subsequent heating and expansion has been proposed by Bettis, House, and Guenther as the damage mechanism in solids. Based on this premise, they have demonstrated the damage intensity threshold to be inversely proportional to the square root of pulse duration and inversely proportional to focused spot diameter (Ref 22).

Shock Wave

The explanation of the shockwave associated with plasma formation follows a number of theories. The types of waves theorized include a detonation wave driven by plasma absorption, and a radiation transport wave whereby the radiated thermal energy from the plasma ionizes material behind the plasma which then readily absorbs laser radiation (Ref 18:68, 70). Regardless of the exact expansion mechanism, it is important to understand the characteristics of the shock wave in materials, especially water, for this project.

Using both Nd-YAG and ruby lasers with peak powers less than 5MW, shock waves at the plasma region of up to 233 kbars with velocities of 0.7 cm/sec have been reported. These values seem fairly consistent throughout the literature (Ref 23:282; 24:46). With the pressure wave assumed to radiate outward radially from the plasma, a $1/r^2$ dependence

can be predicted in a homogeneous medium where r is the distance from the plasma center to the pressure wave front. Thus, with the initial plasma having a radius on the order of 10's of microns, it can be seen that the pressure wave is substantially reduced when distances on the order of millimeters are achieved--in other words, distances comparable to those needed for the wave to reach the retina from a plasma formed at the posterior capsule. The exact pressure amplitude of a wave needed to cause retinal damage has not yet been determined. But the work of Aron-Rosa and of Fankhauser and van der Zypen on human subjects has shown no retinal damage to any patients, even after multiple laser firings in the eye (Ref 5; 6).

IV. Design Theory

Introduction

A basic understanding of biological reactions in the eye and of plasma physics, and their correlation to laser beam parameters, has been achieved. The goal of this chapter is to create the theoretical basis needed for designing a system which focuses laser radiation in the eye for the purpose of initiating optical breakdown. After a summary of Gaussian optics, analyses will be performed on optical focusing of a Gaussian beam both in air and in the eye.

The results are applicable to any laser system, but are especially important to the one involved in this thesis. This is so because the design of the focusing optics represents one of the few system parameters not fixed by the given laser. Hence, the analyses of this chapter will be important in designing the focusing optics.

Focusing of a Gaussian Beam

When a laser emits a beam of a single transverse mode (TEM_{00}) with a Gaussian intensity profile, the beam is well defined mathematically and easily modeled. In addition, the equations describing the characteristics of the beam as it propagates through an optical system become enormously simplified compared to the propagation of a multiple mode Gaussian beam or a non-Gaussian beam. The design takes advantage of this simplification.

A Gaussian beam can be described as follows. Assuming the beam propagates along the z-axis in the positive z direction, the point z=0 is defined as the location of the beam waist or focus where the spotsize is a minimum and the wavefront is planar. The spotsize or beam radius, w(z), at any position z describes the orthogonal distance from the beam axis to the point where the beam intensity is $1/e^2$ of the maximum intensity which occurs at the beam axis. Finally, the Rayleigh range, z_R, is defined as in Chapter III on page 26. The above definitions are depicted in Figure 5. Note that spotsizes are defined as the radius of the beam and not the diameter.

In order to limit the spatial extent of the plasma formation, the Rayleigh range, which provides a relative measure of the axial extent of the focal volume, should be minimized--thus minimizing the extent in the eye where the laser intensity is above breakdown threshold.

The Rayleigh range is given by

$$z_R=(\pi w_0^2)/\lambda \qquad [1]$$

where w_0 and λ are the beam waist spotsize and wavelength respectively (Ref 25:32). Note the benefit of a reduced focused spotsize when minimizing z_R, enabling a greater power density at the focus for a fixed beam power. Also, when one considers the far field, half angle, beam divergence given by

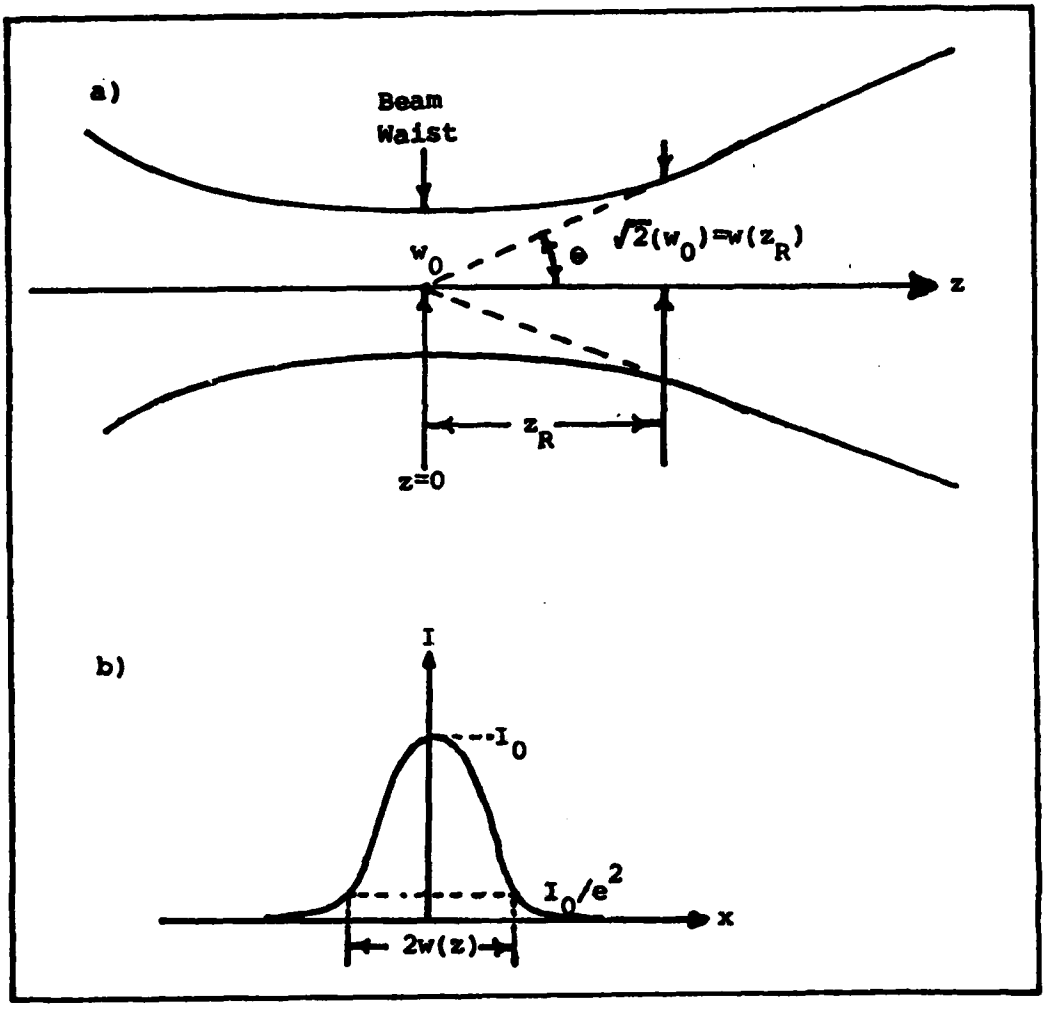

Figure 5. Description of a Gaussian Beam
(a) Beam cross section
(b) Beam intensity (I) profile

$$\theta=\lambda/(\pi w_0) = w_0/z_R \text{ rad} \qquad [2]$$

(Ref 25:33) it becomes evident that the beam spread becomes larger for decreased z_R. The larger beam spread provides yet another benefit, namely a greater rate of reduction of beam intensity with distance from the focus and hence a lower risk of damage to parts of the eye both forward of and behind the focus. In other words, any decrease in z_R

implies a smaller beam waist and a larger divergence (or convergence due to symmetry about z=0).

It can also be shown that by focusing a Gaussian beam with a lens of focal length f, the relationship of the focused waist spotsize (now referred to as w_{02}) to the unfocused waist spotsize, w_{01}, is given by

$$(1/w_{02})^2=(1/w_{01}^2)(1-(z_1/f))^2+(1/f^2)(\pi w_{01}/\lambda)^2. \qquad [3]$$

Here z_1 is the distance from the unfocused waist to the lens. The parameters of Equation 3 are illustrated in Figure 6. Equation 3 illustrates (after close examination)

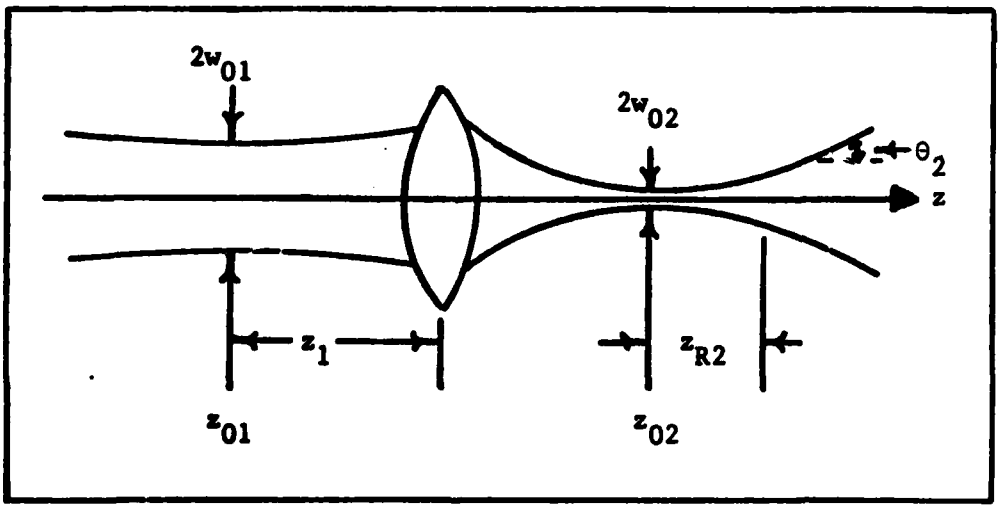

Figure 6. Focusing of a Gaussian Beam

that the larger the waist of the beam incident on the focusing lens (w_{01}), the smaller the focused waist spotsize (w_{02}), and hence the smaller the focused Rayleigh range (z_{R2}). This demonstrates the advantage of expanding the

initial laser beam before focusing it in the eye. After the focused spotsize is calculated, the spotsize at a distance z from z_{02} is given by

$$w(z)=w_{02}[1+(\lambda z/(\pi w_{02}^2))^2]^{\frac{1}{2}} \qquad [4]$$

With Equations 1 through 4, one can solve a typical problem to illustrate the effectiveness of beam expansion for λ=1.06μm (Nd-YAG). Beam intensity is calculated at the beam focus and for given intervals of distance beyond the waist for a fixed value of peak power and focal length. The calculations are performed twice, first with a waist size of 0.8247mm for the unexpanded, raw laser beam incident on the focusing lens, corresponding, as will be shown later, to the actual theoretical value for the given system. The second calculation is made using an input beam waist spotsize of 4.1235mm, corresponding to the acutal value of the system's expanded beam associated with a 5x beam expander. For both cases, f=40.95mm. The results are plotted in Figure 7. Note that the expanded beam has a higher peak power density due to the smaller waist size, and a more rapid drop in power density with distance due to the increased beam divergence of the focused beam (θ_2).

Increasing θ_2--either through greater beam expansion (increase w_{01}), reduction in focal length (decrease f), or a combination of the two--to achieve the benefits of a

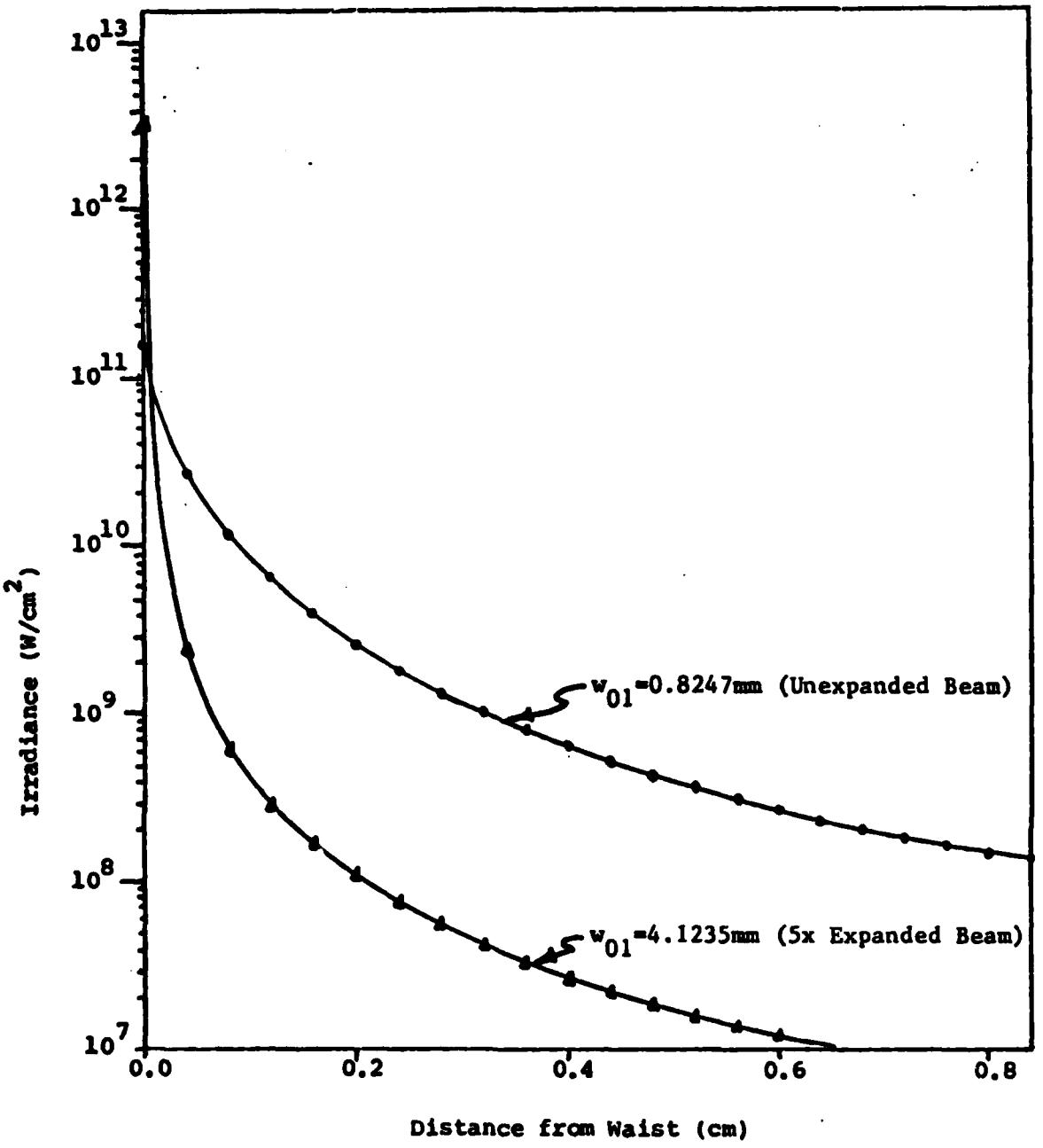

Figure 7. Irradiance vs. Distance from Beam Waist

reduced z_{R2} and w_{02}, has limitations based on two constraints.

The first constraint is based on the effects of the focusing lens on the beam. Note from Equation 3 that the focused waist spotsize, w_{02}, is roughly proportional to

$f/w_{01}=2f\#$. Therefore, if f is decreased or w_{01}, increased in order to achieve a larger θ_2, the f# is decreased. But decreasing the f# also increases the magnitude of the longitudinal spherical aberration function for simple lenses, creating the possibility of extending the plasma region, as described in Chapter III, if certain precautions are not taken. Recall that extending the plasma region leads to imprecise focusing on the posterior capsule.

The second constraint, which sets an upper limit on the value of θ_2, occurs when the beam is moved from focusing in air to focusing in the eye. Because of the importance of the second constraint, it will be described in detail below.

Beam Focusing in the Eye

The second constraint is based on the limiting aperture created by the iris. Before analyzing this constraint, some new notation will be defined.

Because of the symmetry of the Gaussian beam in air about the z=0 point (the beam waist), the far field beam divergence equals the far field beam convergence. Thus, referring to Figure 6, when focusing a Gaussian beam in air, the far field half angle of convergence = θ_2. Henceforth, this angle of convergence will be called the focusing beam cone half angle and the full angle of convergence will simply be called the cone angle. When focusing the beam in the eye, the refractive effects of the cornea and lens cause a difference between the cone half angle into the eye

and the beam divergence beyond the focus located in the vitreous. Increasing the cone angle at the corena will still produce the desired effects in the eye of a small Rayleigh range and small focused spotsize.

The focusing cone half angle can be increased only to the point where the iris blocks part of the incident beam and runs the risk of being damaged by the laser pulse (see Figure 8).

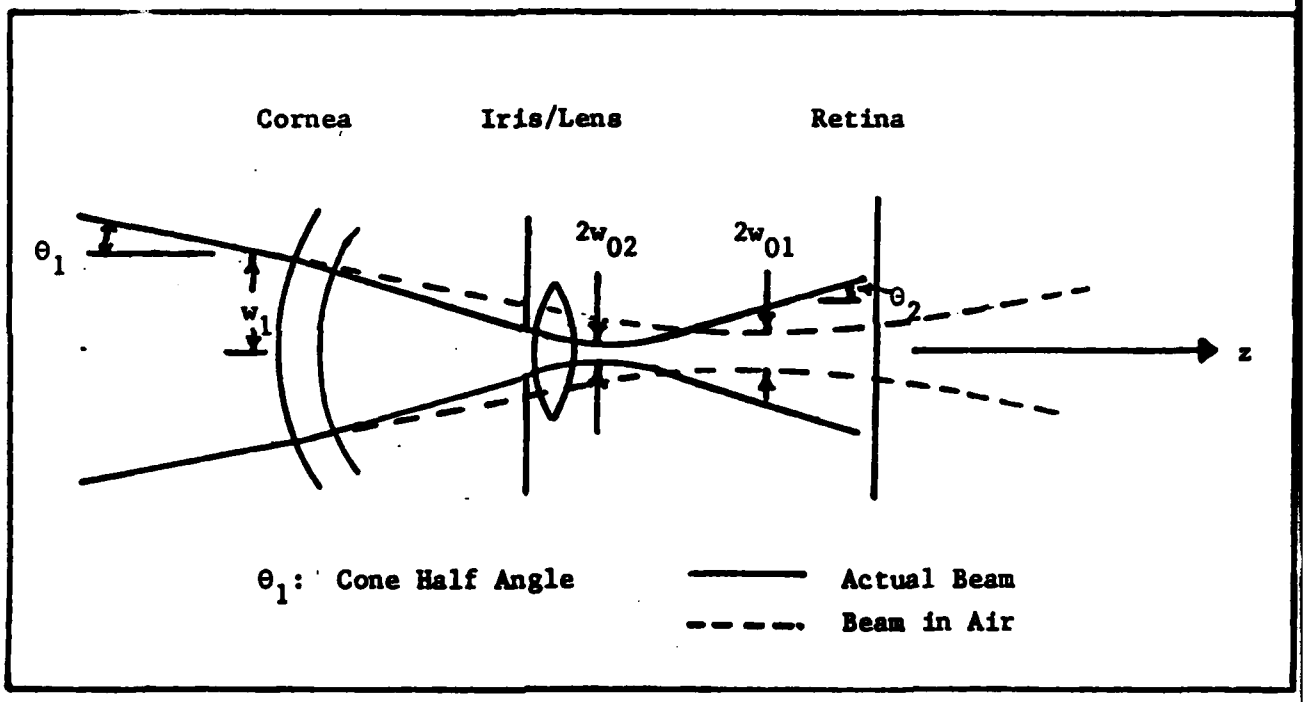

Figure 8. Focusing in the Eye

To evaluate the upper limit on the input beam cone angle at the surface of the cornea, the effect of the eye on the beam must be considered, necessitating the creation of an optical model of the eye.

The eye is modeled rather simply using standard radii of curvature for the corneal surfaces and measured indices

of refraction for the humors and the cornea of a typical adult human eye. A complication arises with the human lens which has a complex structure providing it with an index of refraction which varies with distance and a shape which changes as the eye accommodates to view objects at varying distances. As a simplification, the lens can be assumed to have the homogeneous index of refraction and curvatures given in Figure 9 below which provides an overall optical model of the eye (Ref 26:47).

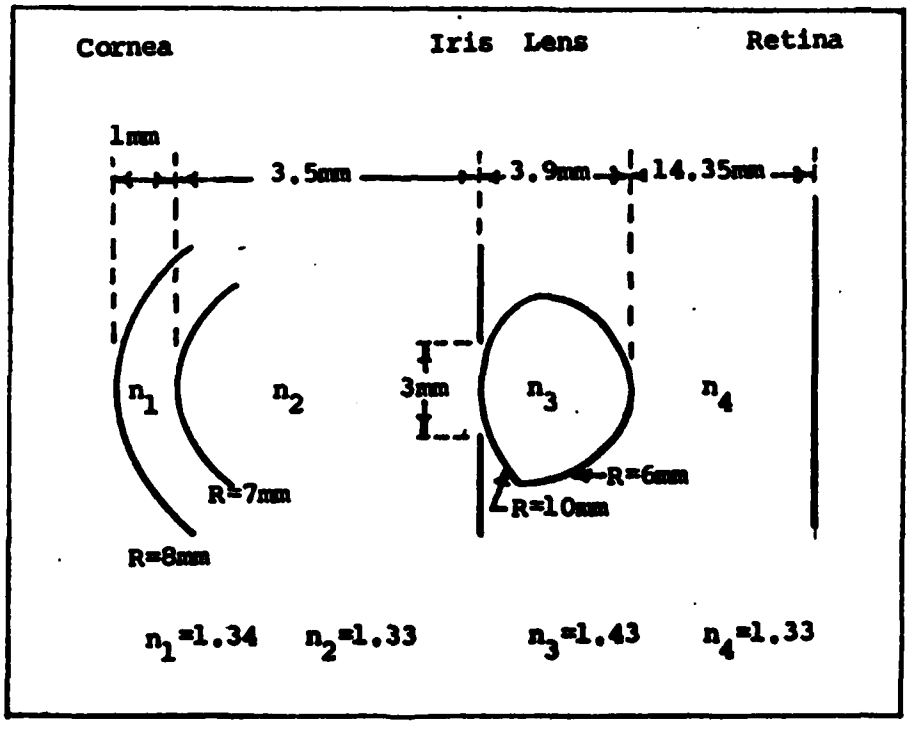

Figure 9. Optical Model of the Human Eye

Note the use of 3mm as the diameter of the pupil. This is a worst case value using the diameter of an undilated pupil. For most patients undergoing treatment, the pupil would normally be dilated to 8mm diameter through the use of certain eye drops; however, a percentage of patients

do not respond to the drug or else have contracted one of a number of diseases which prevents the pupil from dilating. Hence, to insure flexibility of the laser device, it must be designed to handle all possible situations.

Utilizing the above eye model, one wants to find the maximum allowable cone angle in air, at the cornea, for the beam to pass unhindered through the pupil to be focused at a given point between the posterior capsule and the retina. In addition to providing design constraints on a system to open the posterior capsule, this analysis will enable one to study the feasibility of using the laser system to break vitreous strands which occur anywhere between the lens and the retina.

This analysis, using matrix techniques (Ref 32), is based on solving a set of simultaneous equations created by the constraints of a 3mm pupil diameter and the location of the final beam focus at a distance, d, behind the posterior capsule. The use of Gaussian optics proved to be unexpectedly cumbersome due to the propagation of complex variables required to describe the laser beam, and demonstrated the need for simplifying approximations. The approximation chosen used geometrical ray optics to solve for the maximum input ray angle for a given location of the geometrical focus behind the posterior capsule. A determination of the accuracy of this assumption is crucial. The justification is provided below in general terms with the details provided in Appendix A.

The distance from the output of an optical system described by the 2x2 ray trace matrix, $\begin{bmatrix} A & B \\ C & D \end{bmatrix}$, to both the geometrical ray focus and Gaussian beam focus (waist) will be found and compared. This method is depicted in Figure 10 below.

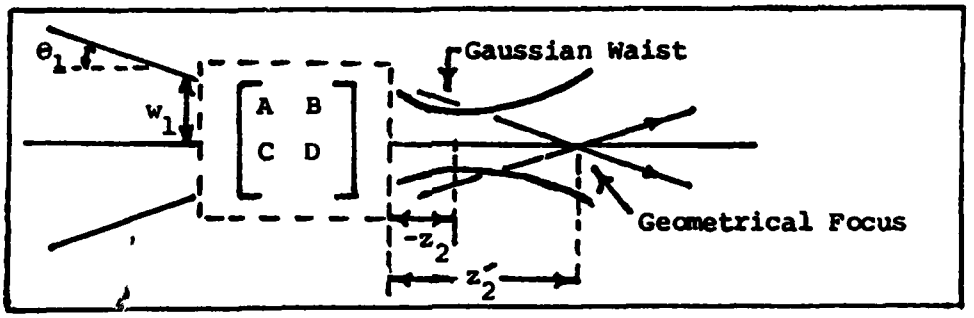

Figure 10. Model used in Analyzing the Geometric Approximation

For the following derivation, the subscript "1" refers to the beam incident on the optical system. Therefore, z_{R1} and w_{01} refer to the Rayleigh range and waist spotsize of the incident beam as if it were focused in air and not transmitted through the system (see Figure 8, page 38). The subscript "2" refers to the output beam from the optical system. For the geometrical case, the distance z_2' for the location of the geometrical focus from the system output is found (Appendix A) to be

$$z_2' = \frac{A(w_1/\theta_1)-B}{-C(w_1/\theta_1)+D} \qquad [5]$$

This result rests on the assumption that the input to the

system is in the far field (i.e. the ray angle and elevation are equivalent to the input cone angle of the Gaussian beam (θ_1) and Gaussian spotsize (w_1) at the input to the system). For the Gaussian case, it can be shown (Appendix A) that

$$-z_2+jz_{R2}=\frac{A(-z_1+jz_{R1})+B}{C(-z_1+jz_{R1})+D} \qquad [6]$$

By multiplying both numerator and denominator of the right side of Equation 6 by the complex conjugate of the denominator and equating real parts, it is found that

$$z_2=\frac{(Az_1-B)(-Cz_1+D)-z_{R1}^2AC}{(-Cz_1+D)(-Cz_1+D)+z_{R1}^2C^2} \qquad [7]$$

where z_{R1} is the Rayleigh range of the input beam. By again assuming operation in the far field, the square of the waist spotsize of the input beam, w_{01}^2, is much smaller than w_1^2, and

$$z_1^2=(w_1^2-w_{01}^2)(1/\theta)^2\cong(w_1/\theta)^2 \qquad [8]$$

Substituting this result into Equation 5 yields

$$z_2'=\frac{Az_1-B}{-Cz_1+D} \qquad [9]$$

At the same time, the condition, $w_{01}^2 << w_1^2$, implies $z_{R1}^2 << z_1^2$ by Equation 1, so Equation 7 becomes

$$z_2 \cong \frac{(Az_1 - B)}{(-Cz_1 + D)} = z_2' \qquad [10]$$

Thus, it has been shown that the geometric approximation is valid with the assumption $w_{01}^2 << w_1^2$, a condition which would be met anyway, as stated earlier, in order to minimize the focal volume.

With knowledge that the geometrical approximation is valid for laser beam propagation, the calculation of maximum cone angles allowable when irradiating the eye can proceed as follows. Using the optical model of Figure 9, and labeling the input plane of the cornea as reference plane (RP)0, the plane of the iris as RP1 and the focal plane behind the lens as RP2; the matrix associated with light propagation the eye from the surface of the cornea to the plane of the iris is

$$M_1 = \underbrace{\begin{bmatrix} 1 & 2.556 \\ 0 & 1 \end{bmatrix}}_{\text{Anterior Chamber}} \underbrace{\begin{bmatrix} 1 & 0 \\ 1.4286\times10^{-3} & 1 \end{bmatrix} \begin{bmatrix} 1 & 0.746 \\ 0 & 1 \end{bmatrix} \begin{bmatrix} 1 & 0 \\ -4.25\times10^{-2} & 1 \end{bmatrix}}_{\text{Cornea}}$$

$$= \begin{bmatrix} +0.8632 & 3.305 \\ -0.04113 & 1.001 \end{bmatrix} \qquad [11]$$

The matrix describing light propagation in the eye from the cornea to a distance, d, behind the posterior capsule is given by

$$M_2 = \underbrace{\begin{bmatrix} 1 & d/1.33 \\ 0 & 1 \end{bmatrix}}_{\text{Vitreous}} \underbrace{\begin{bmatrix} 1 & 0 \\ -0.01667 & 1 \end{bmatrix}\begin{bmatrix} 1 & 2.727 \\ 0 & 1 \end{bmatrix}\begin{bmatrix} 1 & 0 \\ -0.01 & 1 \end{bmatrix}}_{\text{Lens}} M_1$$

$$= \begin{bmatrix} (0.7275 - 0.04655d) & (5.944 + 0.6531d) \\ -0.06191 & 0.8687 \end{bmatrix} \qquad [12]$$

At the plane of the iris the ray vector is given by

$$\begin{bmatrix} Y_1 \\ V_1 \end{bmatrix} = M_1 \begin{bmatrix} Y_0 \\ V_0 \end{bmatrix}$$

or

$$Y_1 = +0.8632Y_0 + 3.305V_0 \qquad [13]$$
$$V_1 = -0.04113Y_0 + 1.001V_0$$

Here we are using the convention that the elements Y_i and V_i are the ray height above the optical axis and reduced ray angle in radians, respectively, at a given point along the optical axis, as shown in Figure 11 page 45. Similarly,

$$\begin{bmatrix} Y_2 \\ V_2 \end{bmatrix} = M_2 \begin{bmatrix} Y_0 \\ V_0 \end{bmatrix}$$

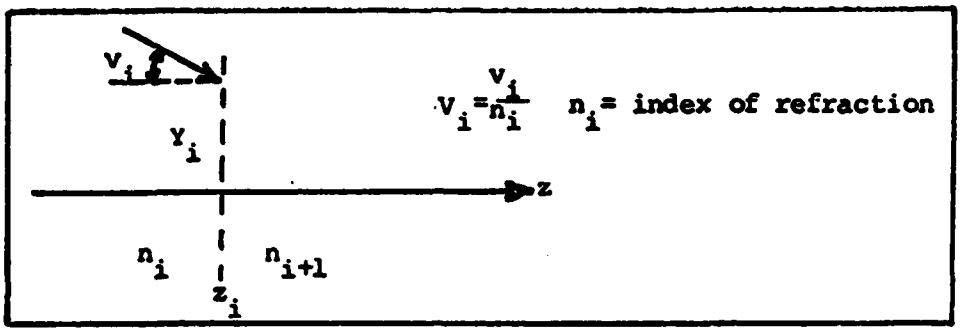

Figure 11. Description of Ray Vector

or

$$Y_2 = (0.7275 - 0.04655d)Y_0 + (5.944 + 0.6531d)V_0$$
$$V_2 = -0.06191Y_0 + 0.8687V_0$$

Applying the constraints of a 3mm diameter pupil (Y_1=1.5mm) and a focus at distance d behind the capsule (Y_2=0), and solving for the input cone half angle, $v_0 = V_0/n_i$ (n_i=index of refraction at location i) gives

$$v_0 = \frac{V_0}{1} = \frac{(0.08089d - 1.2642)}{(0.83133d + 3.1586)}. \qquad [14]$$

Equation 14 is graphically depicted in Figure 12 on page 46.

An analysis of Figure 12 indicates a rapid reduction of allowable input cone angles when moving the focus from the capsule toward the retina. At the posterior capsule the full output cone angle is approximately 45°; at a distance 15mm further on toward the retina, the cone angle

has dropped to several degrees. While the error of this analysis increases with distance d as the geometrical ray optics approximation becomes more and more invalid (i.e. w_{01} approaches w_1), it is clear that attempting to create a

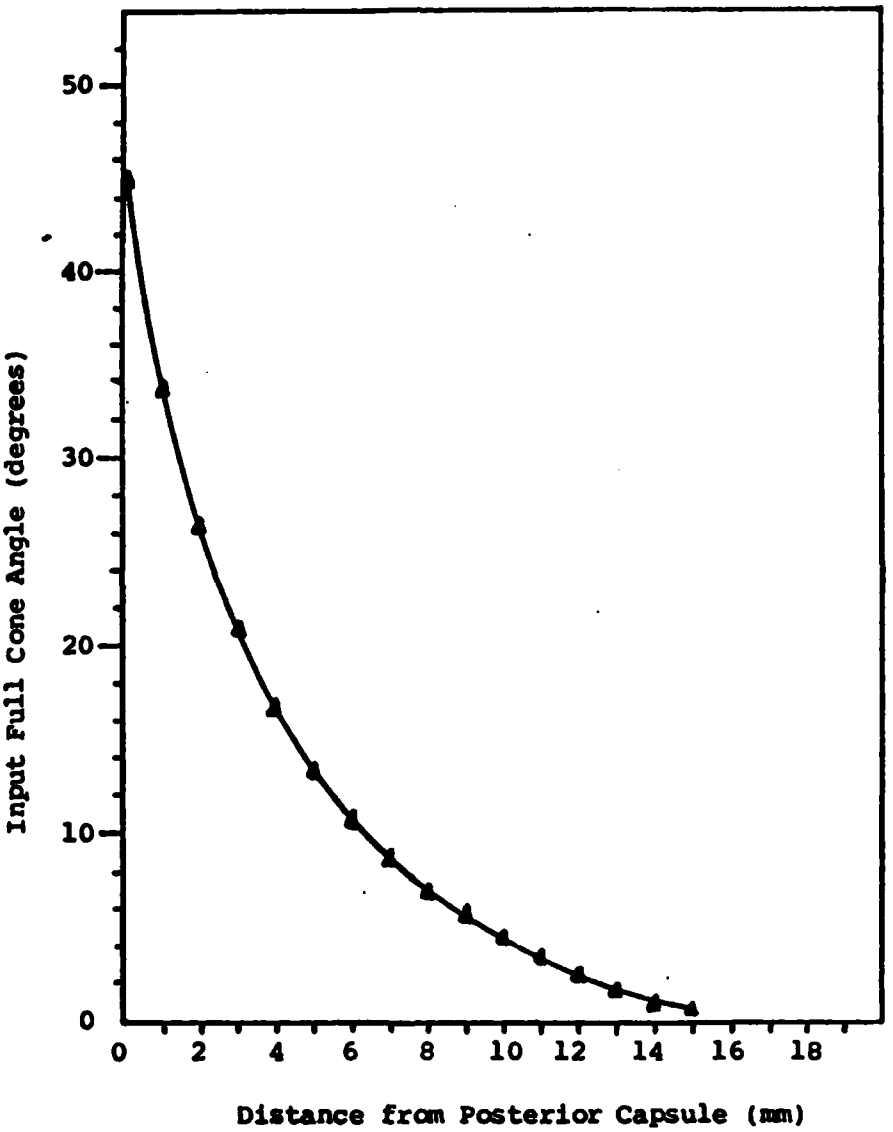

Figure 12. Maximum Allowable Cone Angle at Cornea Consistent with a Focus Behind the Posterior Capsule

breakdown plasma more than a few millimeters behind the capsule is not very feasible. Appendix B describes in

detail an extension of the above analysis to calculate the corresponding spotsize, w(z), incident on the retina when the laser is focused at various distances d_i given in Figure 12. Figure 13 is a plot of the results of this extension.

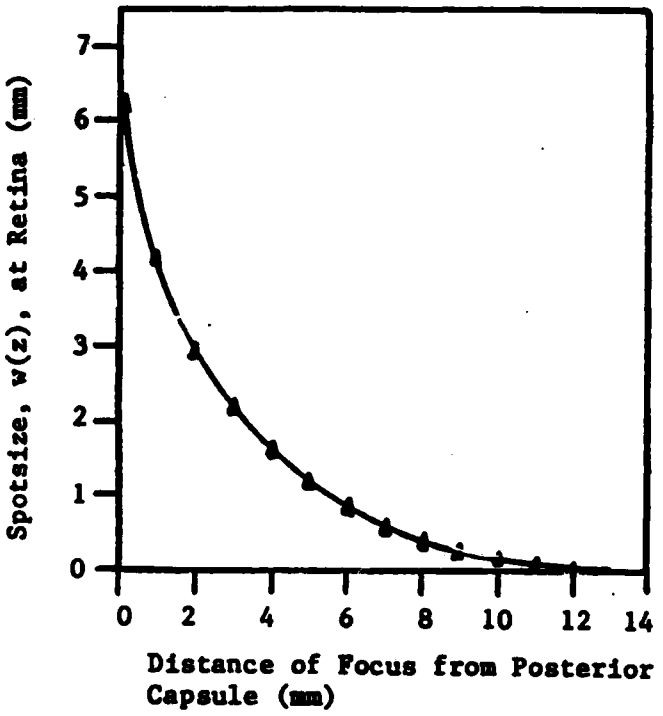

Figure 13. Retinal Spotsizes Resulting from Focusing Behind the Posterior Capsule with Maximum Input Cone Angle

Note especially the small spotsizes of the laser beam striking the retina as the laser beam is focused farther and farther beyond the posterior capsule. Such small spotsizes clearly mean high power densities on the retina, leading to potentially grave retinal damage.

V. System Design and Theoretical Performance

The experimental set up, as shown in the schematic of Figure 14, consists of a high power Nd-YAG laser beam propagating collinearly with a low power He-Ne aiming beam. The two beams pass through an adjustable attenuator and flexible articulated arm on their way to the ophthalmic slitlamp. The focusing optics--a beam expander and lens system--are used to focus the two beams on the target. The beam expander, lenses, and target are all mounted on the slitlamp which contains, in addition, an adjustable binocular system for viewing the breakdown phenomena in test cells and eyes.

Lasers

The primary laser, the Nd-YAG, is a Quantel Model YG482cm, consisting of one resonator and two amplification stages. Since the beam is normally highly diffracted after passing through the amplifier stages, resulting in a non-Gaussian intensity profile, only the resonator stage was utilized. Sacrificing the amplifier stages led to a large decrease in output power, but guaranteed a TEM_{00} beam profile. Since the theoretical calculations are all based on a TEM_{00} Gaussian beam, the results would only be meaningful with that condition met.

The resonator cavity is plano-concave, of length 107cm with a 7mm diameter x 90mm long Nd-YAG rod spaced 53.5mm from the plane (output) mirror. The rear mirror consists

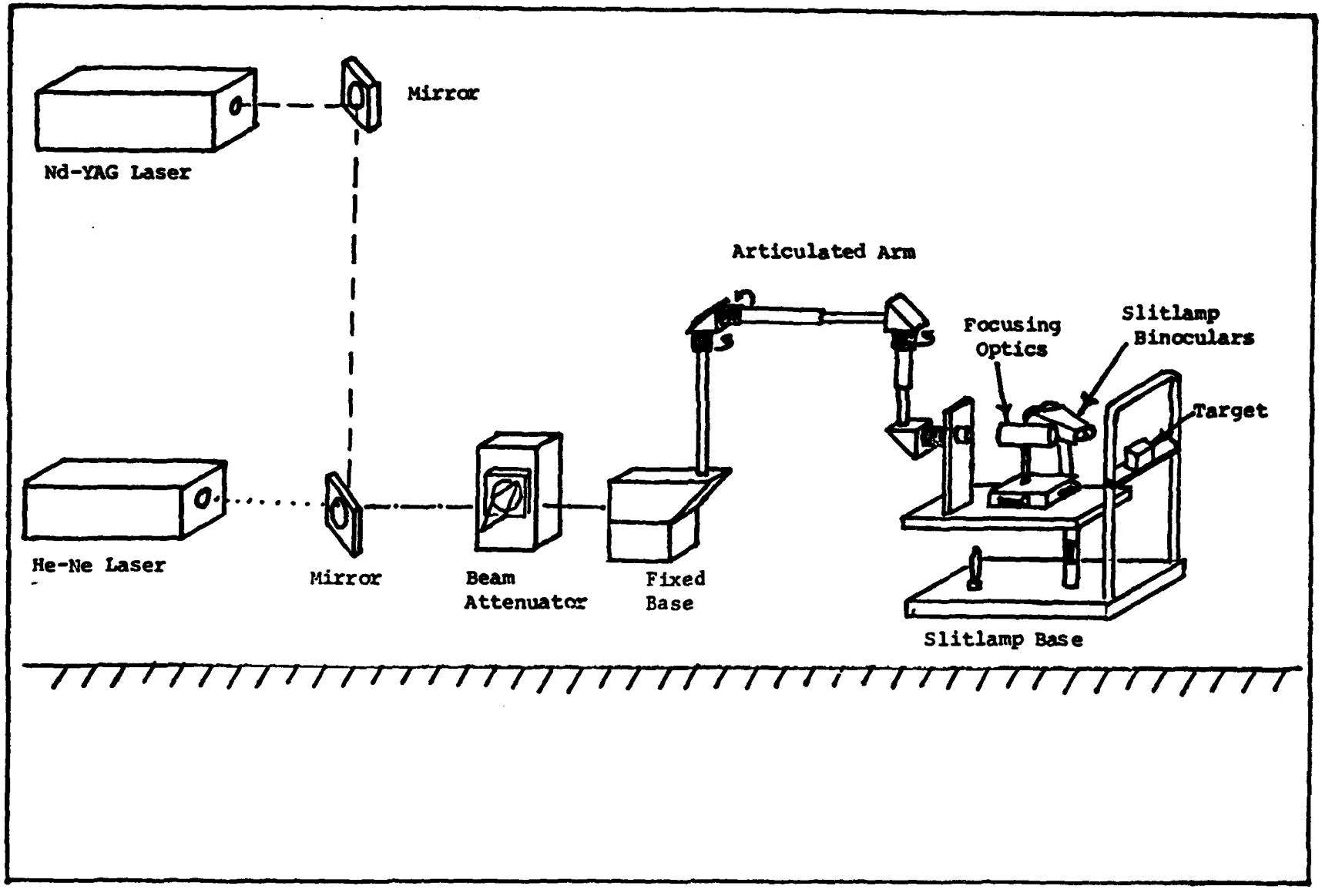

Figure 14. System Schematic

of high reflective (HR) coated fused silica with a 5m radius of curvature (R_1) and a diameter (D_1) of 2.1cm.

The output mirror is of flat-flat fused silica design with thickness t=8mm and diameter D_2=2.1cm. The laser is actively Q-switched by a Pockel's cell mounted between the rod and rear mirror. An aperture between the Q-switch and the rod provides selection of the TEM_{00} mode. The laser cavity is schematically depicted in Figure 15.

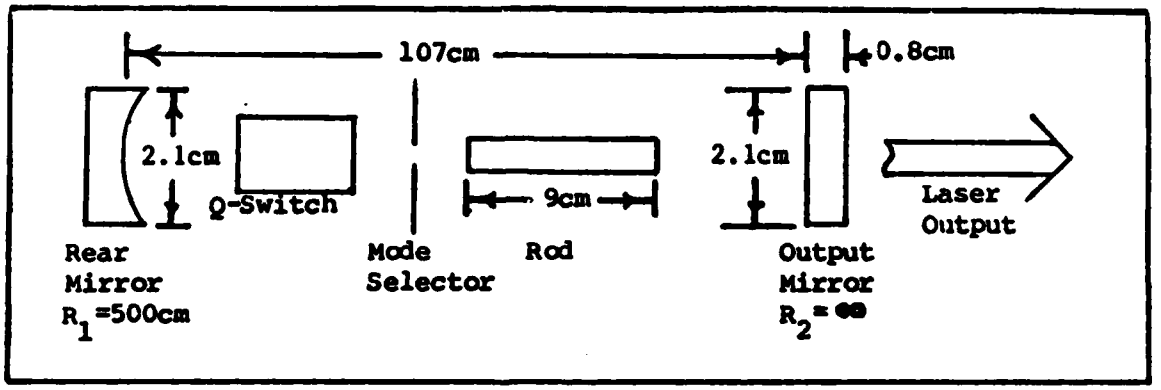

Figure 15. Nd-YAG Laser Cavity

The theoretical analyses of the beam parameters, which follow at the end of this chapter, are based on the propagation of a spherical Gaussian TEM_{00} beam and are only accurate when the spotsizes at the resonator mirrors are smaller than the mirrors themselves, thus eliminating diffraction problems. If one makes use of Equation 15, a relationship between the transmitted power (P) and the total power (P_0) incident on an aperture of radius "a", for a TEM_{00} Gaussian beam of spotsize w at the aperture,

$$\frac{P}{P_0} = 1-\exp(-2a^2/w^2) \qquad [15]$$

one can show that so long as $a \geq 1.5w$, 99% of the incident energy is transmitted by the aperture, and no additional diffraction effects are introduced by the aperture (Ref 25:35). The spotsizes at the rear mirror and output mirror, respectively, are given by (Ref 25:30)

$$w_1 = [L\lambda/\pi]^{1/2}\left[\frac{g_2}{g_1(1-g_1g_2)}\right]^{1/4}$$

$$w_2 = [L\lambda/\pi]^{1/2}\left[\frac{g_1}{g_2(1-g_1g_2)}\right]^{1/4} \qquad [16]$$

where

$$g_1 = 1-L/R_1 \text{ and } g_2 = 1-L/R_2 \qquad [17]$$

where L is the reduced length of the cavity, that is, the actual length adjusted for the different indices of refraction of the rod, polarizers, and Q-switch crystal. For this resonator, L=101.1cm.

For the given laser Equation 16 yields, w_1=0.9233mm and w_2=0.8247mm. Upon inspection, then, since "a" for each is 10.5mm, the cavity mirror limitation $a \geq 1.5w$ is well met.

Two 100% reflecting sapphire mirrors deflect the Nd-YAG beam to the input of the articulated arm. Through

the second mirror, a beam from a Spectra Physics Model 132-01, 5mW He-Ne laser is directed such that at the reflecting surface, the two beams become collinear.

Beam Attenuator

Because of difficulty locating a commercial beam attenuator capable of handling the high projected peak power densities of the laser, a "laboratory" version was improvised using a thin glass microscope slide rotatable on a horizontal axis (perpendicular to the optical axis) through a known angle between 0° and 50°. The beam attenuation which occurs is given accurately by the Fresnel equations which describe the percent of reflected and transmitted light for any angle of incidence for any dielectric interface. The exact equations which describe the reflectance as a function of angle of incidence were not needed for the given system because the attenuator was physically calibrated by measuring transmitted energy as a function of angle of rotation of the glass slide.

Articulated Arm

For a laser beam to be useful as a surgical tool, it must be accurately translatable in three dimensions, enabling the user to quickly and precisely vary the aim point of the laser. Laser surgical system designs generally utilize two different beam transfer mechanisms; fiber optics for relatively low power systems, or a flexible system of mirrors known as an articulated arm. Because of

the higher reliability, and virtual lack of alignment problems, a fiber optic system was investigated for use in the system and a brief explanation follows as to why this alternative was ultimately dismissed.

The feasibility study was based on two criteria. First, the fiber or fiber bundle must be able to handle peak power densities of 10MW/cross sectional area of the fiber. Secondly, pulse power and both temporal and spatial beam characteristics must not be severely degraded. The first criterion has been shown to be possible (Ref 28) in unglued 5mm diameter fiber bundles of a silica core where input power densities for λ=1.06μm of up to 1.61 GW/cm^2 were successfully transmitted. However, for a single fiber of cross section 40.7x10^{-6}cm^2, the input power density limit would be exceeded.

The second criterion, however, even with a fiber bundle, cannot be met. The diffraction effects of a fiber bundle, acting as an array of circular apertures, would produce an output beam far removed from a pure TEM_{00} mode--on which present calculations are based--and at the same time inhibit the ability to focus down to as small a spot as desired. For this reason, an articulated arm, rather than a fiber optic bundle, was used in the system design.

The articulated arm used in the present system was a modification of an existing arm designed for use in CO_2 corneal surgery (Ref 2:36-38). The arm consisted of a

fixed base with a mirror set at 45° from the vertical, three 90° elbows with adjustable 45° mirrors, and interconnecting tubing. The first vertical member was rigid while the horizontal and second vertical member were telescoping with two elements each. A schematic of the complete arm is shown in Figure 14 on page 49. The base, elbows and outer sheathing of the telescoping arms were constructed of lightweight aluminum, the rest of the tubing of stainless steel for rigidity. Connecting one of the two tubes at each elbow with a bearing, provided the range of motion needed for the interface of the arm with the slitlamp. All openings and tube diameters were much larger than needed to satisfy the $a \geq 1.5w$ criterion discussed earlier.

Highly polished copper (to 1λ) was used for the mirrors due to its availability and high reflectance (98%) at 1.06μm. The disadvantage of using copper lies in its susceptibility to surface oxidation which degrades system performance with time. HR coated dielectric mirrors--which had been ordered but arrived too late to be incorporated in the system--offer greater individual reflectance and eliminate the oxidation problems.

Focusing Optics

At the output of the articulated arm, the He-Ne and Nd-YAG laser beams are directed through a beam expander-lens combination, to provide a smaller focused spotsize than would otherwise be possible with an unexpanded beam.

The beam expander, being a preconstructed unit from an unrelated system, was of unknown optical material and expansion power, and required an analysis to determine these parameters. Assuming the optics to be of either optical crown or optical flint glass, the difference in the index of refraction between He-Ne wavelength of 632.8nm and Nd-YAG wavelength of 1064nm is small enough to conclude that the properties of the expander using either beam are virtually the same. Using the He-Ne laser, the beam expander was determined to be a 5x expander with a negative meniscus input lens of focal length -2.35cm and a convex-convex output lens of focal length 10.8cm. As will be seen in a following subsection, the 7mm diameter input aperture satisfied the $a \geq 1.5w$ criterion.

A focal length of >35mm for the final lens system was chosen to provide as large an input cone angle as possible (up to the limits set in Figure 12) while still allowing a reasonable working distance between the lens and the test targets.

The initial lens chosen and utilized was an achromat lens doublet with f=40mm providing nearly zero spherical aberration at λ=1.06μm. Both glued and unglued doublets were used, and both failed through fracture after only a few laser shots. The cause of failure was determined to be a relatively high impurity concentration in the flint glass portion of the crown-flint combination. The system finally used contained a pair of plano-convex lenses constructed of

high purity BK-7, and oriented with convex surfaces in contact. The individual lenses each have a focal length, f=81.91mm, giving the combination a focal length of 40.95mm at 1.06μm compared to a combination focal length of 40.28mm for 632.8nm light. Both lenses have a diameter of 22mm. A schematic of the focusing optics is presented in Figure 16.

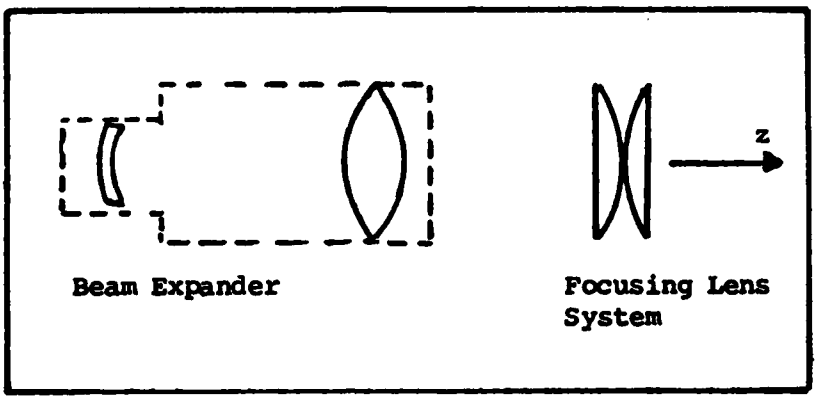

Figure 16. Focusing Optics

Test Cells

A majority of the experimentation involved firing the laser through an artificial lens implant suspended in water on a simulated posterior capsule at a known distance from the focusing optics. This series of experiments required the construction of a specialized test cell.

The cell was constructed of transparent Plexiglas with the exception of the two faces in the path of the beam which were constructed of glass. A removable plastic frame holding the target (a small sheet of plastic) could be inserted in the cell in the path of the beam. The removable lid of the cell was slotted to allow movement of a plastic slide, which holds the IOL, along the direction of the

optical axis. The slide was kept under tension by two springs while being pushed by a fine threaded screw which provided movement of 0.025"=0.635mm per rotation. The test cell is illustrated in Figure 17 below and a detailed drawing is provided in Appendix C.

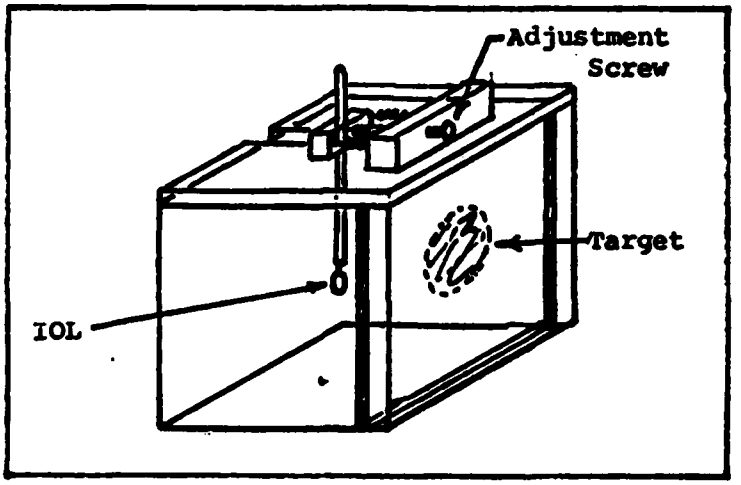

Figure 17. Test Cell

A second prefabricated cell was also used. This cubical glass cell, smaller than the specialized cell described above, measured approximately 2.5mm along an edge and was used to hold various fluids on which breakdown threshold measurements were conducted.

Theoretical Beam Analysis

Having discussed the system components, a theoretical analysis of the beam parameters at different points in the system will be performed using matrix optics techniques to propagate the TEM_{00} Gaussian beam from its theoretical

waist location at the cavity side of the laser output mirror.

The system can be modeled as shown in Figure 18. For the calculations to follow, all lengths are in cm.

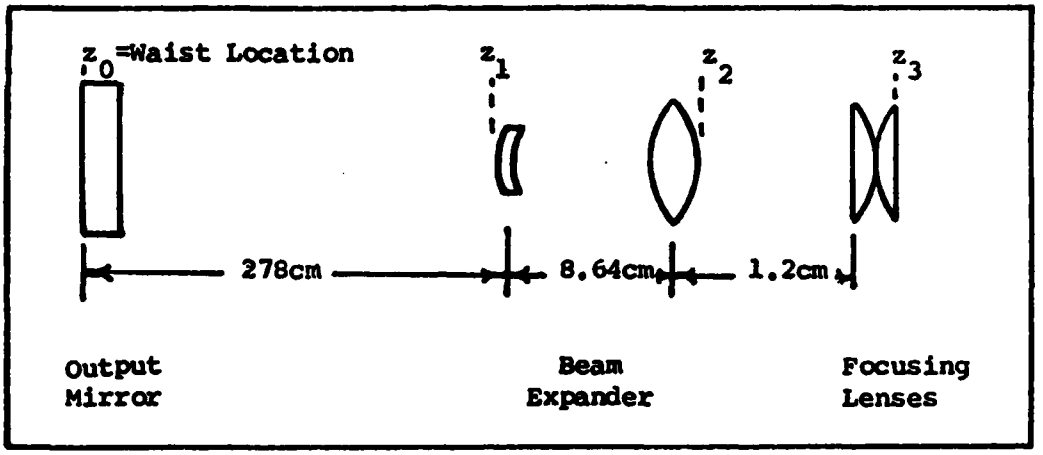

Figure 18. Laser System Model

The spotsize at z_1, the entrance of the beam expander is determined from Equation 4 by letting z equal the reduced path length between z_0 and z_1. The result is $w(z_1)$=0.14091cm. Thus, the 2.82mm beam diameter at z_1 is well within the $a \geq 1.5w$ criterion for the 7mm aperture of the beam expander.

Using the matrix which describes the system from z_0 to z_2, the output of the beam expander, values for the waist spotsize, divergence, and waist location (z_{02}) of input beam to the focusing lens were found to be w_{02}=0.41235cm, $\theta_3=\lambda/(\pi w_{02})$=82.130 rad, and z_{02}=-6998.8cm. The negative z_{02} implies that the waist of the output beam from the beam

expander is virtual and located z_{02} cm to the left of z_2.

With this information, Equations 2 and 3 can be applied to the focusing lens with the results,

$$W_{03}=1.9612\mu m$$
$$\theta_3=9.894°$$
$$z_{R3}=11.357\mu m$$

Note that the values found for z_{02} and w_{02} are those used for one of the curves in Figure 7 on page 36.

The results of the above analysis, then, predict a focused spot diameter of 3.922μm with an 11.357μm Rayleigh range in air. These values will not vary significantly when focusing in the fluids of the test cell, but will differ when focusing in the eye due to the effects of the curved cornea and lens on the complex radius of curvature of the focusing beam. The above values of the beam parameters in air can be extended to the case of focusing in the eye through the use of the beam divergence value, θ_3, and the graph and associated equations of Figure 13.

The value of the aberration function for the focusing lens is worked out in detail in Appendix D and yields a value of 4.9λ. Note the comparison with the value for a single plano-convex lens of f=40mm which is 10.1λ, where the plano-convex shape is optimal for single lenses without resorting to aspherics. Therefore, the lens combination does yield better performance than the single lens but is

still approximately five times larger than the 1λ criterion discussed in Chapter III. This discovery, however, was made too late in the experimentation to modify the system to a less severely aberrated form. The calculations of the focused spot diameter and hence calculations of threshold intensity values will be accurate; however, the use of the Rayleigh range as a measure of the length of the focal area will theoretically suffer slight inaccuracies due to the longitudinal spherical aberration, the exact amount of which was not calculated.

The final theoretical analysis involves the determination of the difference between the focal lengths of the focusing lens for the Nd-YAG beam and for the He-Ne beam. The importance of this calculation is that it will give an indication of the location of the Nd-YAG focus when the He-Ne focus is placed at a given spot in the eye.

The two values for the indices of refraction for BK-7--n=1.50664 at λ=1.064μm and n=1.51509 at λ=632.8nm--along with the value for the radius of curvature for the individual lens (41.4978mm), gives the desired results. For the Nd-YAG beam, f=40.9539mm and for the He-Ne beam, f=40.2820mm, where the given focal length is for the lens combination. The closeness of the two values indicates that the difference in focus locations when irradiating the eye is on the order of hundreds of microns, much less then the precision to which the ophthalmologist

can focus the He-Ne beam and less than the uncertainties of the location of the plasma formation.

VI. Experimental Procedures and Results

Introduction

The experimental procedures consisted of a measurement of beam parameters with a comparison to the expected values calculated in Chapter V followed by a series of tests on the effects of the beam on a newly developed glass IOL.

Beam Parameter Measurements

The results of all the beam effects tests depend on accurate knowledge of the beam pulsewidth, energy, and focused spot diameter.

The pulsewidth was measured using an EG&G Model 580 radiometer detector head with narrow beam adapter, externally biased with -940VDC, to detect scattered radiation from an illuminated glass microscope slide placed at the output of the focusing lens. The resultant signal, displayed on a Tektronix Model 7904 oscilloscope with a Model 7A16A input amplifier module and a Model 7B92 time base module, indicated a full width at half maximum time of 27ns (see Figure 19).

The EG&G Model 580 radiometer and narrow beam adapter was also used for measurement of pulse energy, after a precision calibration was performed at the start of the experimental work. All pulse energies listed in the remainder of the paper have a maximum standard deviation value of ±4.5%. This value is a combination of the errors arising from the radiometer calibration and the maximum

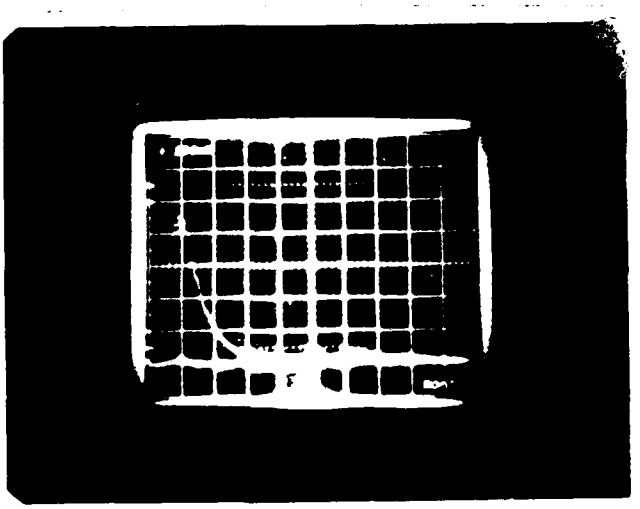

Figure 19. Output Pulse Shape

random error calculated from a twenty shot average value for each measurement.

Pulse energies were not measured during the actual experimental testing. Rather, energies measured at a given laser lamp voltage setting and at 10° increments of beam attenuator angle before the tests began, were used. A beam energy check midway through the testing revealed no discrepancies with the initial measurements. The maximum pulse energy available at the output of the slitlamp optics, with a 0° attenuator setting and 2.0KV to the laser lamp, was found to be 10.89mJ.

The most difficult of the beam parameters to measure is the focused spotsize in air. The high peak power density and a spotsize on the order of microns rendered thermally sensitive photographic paper useless. The measured values of 80-200 μm on thermal paper were probably

caused by a "bleeding" from the large energy densities at the focus. The use of photographic paper with no thermal response at 1.06μm was also attempted, resulting in an impact area of fiber damage with a central perforation. The minimum spotsize diameter obtained with this method were 28.58μm for the outer damage area with a 10.71μm perforation. The obvious question--which of the two figures, if either, corresponds closest to the $1/e^2$ intensity points of the beam--could not be answered until an alternative, definitive method could be found.

The method decided upon was an indirect application of a technique proposed by Yoshida and Asakura (Ref 28) whereby an opaque ribbon is placed centrally in the path of the beam and the $1/e^2$ intensity points are determined mathematically from the ratio of transmitted power to incident power. For the given system a ribbon could not be placed at the beam focus. Alternatively, two measurements were obtained well into the far field beyond the focus, at a known separation. From these two measurements, the far field divergence of the beam was calculated geometrically. The waist size could then be calculated from Equation 2. Application of this method resulted in a focused beam diameter of 4.387±0.976μm. The calculations and error analysis can be found in Appendix E.

References to a given pulse energy setting in the experiments described below, will be followed by a peak

energy density value in parenthesis. The value is based on a 4.4μm focused spot diameter and a 27ns pulsewidth.

Determination of Plasma Formation

It became clear with the first few shots into the test cell filled with tap water, that verification of plasma formation at all energy levels could be made without the aid of instruments. Regardless of the size of the plasma, the brightness was such that it could be seen with the naked eye. The plasma formation was also always accompanied by a distinctive "pinging" sound believed to be due to a resonance of the test cell caused by shock wave formation.

Determination of Breakdown Characteristics

An unexpected question arose from the test on the determination of the plasma. Initially the tests had been planned with a distilled water environment but a change to tap water was made when plasma formation could only be achieved on approximately 25% of the shots in distilled water at maximum power, but on 100% of the shots in tap water at maximum power. The discrepancy was attributed to a higher absorbing impurity concentration in the tap water yielding a greater probability for cascade ionization initiation through thermally created free electrons.

In order to determine a solution which closely models the breakdown characteristics of the vitreous, threshold measurements were made on distilled water, tap water, and

balanced salt solution (BSS), and compared to measurements made on human and pig vitreous.

No attempt will be made to define a precise threshold level for the fluids where plasma formation will occur on 100% of the laser shots because this level was not possible in all the fluids with the limited pulse energy of the given system. The thrust of the experiment, then, is to determine which of the three solutions most closely matches the vitreous with respect to plasma formation.

With the small glass cell used as the test container, the following results were obtained.

In distilled water no plasma formed after fifty shots fired at 1Hz with pulse energies up to 7.89mJ ($1.9 \times 10^{12} W/cm^2$). At the next levels tested, 9.85mJ ($2.40 \times 10^{12} W/cm^2$) and 10.70mJ ($2.6 \times 10^{12} W/cm^2$) plasma formation in both cases occurred on 25% of the shots for series of 50 shots.

In the BSS, the percentage of plasma occurence ranged from 5% at 7.65mJ ($1.9 \times 10^{12} W/cm^2$) to 33% at 10.26mJ ($2.5 \times 10^{12} W/cm^2$). The plasmas were single, cigar-shaped sparks at the lower power density. At pulse energies above 9mJ ($2.2 \times 10^{12} W/cm^2$), the plasmas varied between single sparks 0.1 to 0.25mm long, and multiple sparks of up to 0.75mm.

In tap water, a 100% probability of plasma formation was reached at 5.7mJ ($1.4 \times 10^{12} W/cm^2$), with multiple spark chains 1.5 to 2.0mm long. At 10.3mJ ($2.5 \times 10^{12} W/cm^2$), spark chain lengths reached 2.5mm.

In both pig and human vitreous, and the BSS, plasma formation, for the intensities used, alternated randomly between single and multiple sparks, with the spark chains measuring up to 1.5mm long.

The results of the breakdown characteristics experiment are given in Table II.

TABLE II

Optical Breakdown Characteristics of Certain Fluids

Percentage of 100 Shots on Which Breakdown Occurred

Fluid	Power Density* ($x10^{12} W/cm^2$)				
	0.80	1.4	1.9	2.2	2.5
Distilled Water	0	0	0	0	25
Human/Pig Vitreous	-	-	-	6	32
BSS	-	-	5	7	33
Tap Water	25	100	100	100	100

* Power density based on a 4.4μm focused spot diameter and a 27ns pulsewidth.

- No data obtained.

Effects on Glass IOL

The effects on the glass IOL were conducted in two parts. First, the gross effects were examined by focusing the beam on the IOL suspended in tap water; and second, an investigation of the length of the zone of damage near the plasma was performed by focusing the beam on a target

behind the IOL and gradually moving the IOL toward the target. The purpose of the second experiment was to determine the effects on a glass IOL when focusing on the posterior capsule for different IOL-capsule distances.

To examine the gross effects, the He-Ne beam was focused on the IOL and a single pulse fired. The focus was then moved to a new position on the lens site and five more shots were fired at a 1Hz rate and the damage viewed under the microscope.

At pulse energies up to 9mJ ($2.19 \times 10^{12} W/cm^2$), single shot damage consisted of a circular damage area 70 μm in diameter with three to four radial fractures with lengths up to 300 μm long. In the same energy range, multiple irradiations of up to 15 shots in a single location created damage spots of approximately 900 μm in diameter with many radial fractures. Figure 20 illustrates a comparison of single shot damage to 12 shot damage for 5.67mJ ($1.38 \times 10^{12} W/cm^2$) pulses. Figure 21 illustrates an attempt at determining IOL damage for multiple laser shots focused at different locations on the IOL. The laser beam was focused at a large dark area in the photo and the beam focus gradually adjusted along the optical axis until the effects on the IOL became most violent. At that point, the focus was moved laterally across the IOL, first in one direction and then the other in an unsuccessful attempt at shattering the lens. The energy of the pulses used to create the damage in Figure 21 were 9.0mJ ($2.19 \times 10^{12} W/cm^2$), determined to be

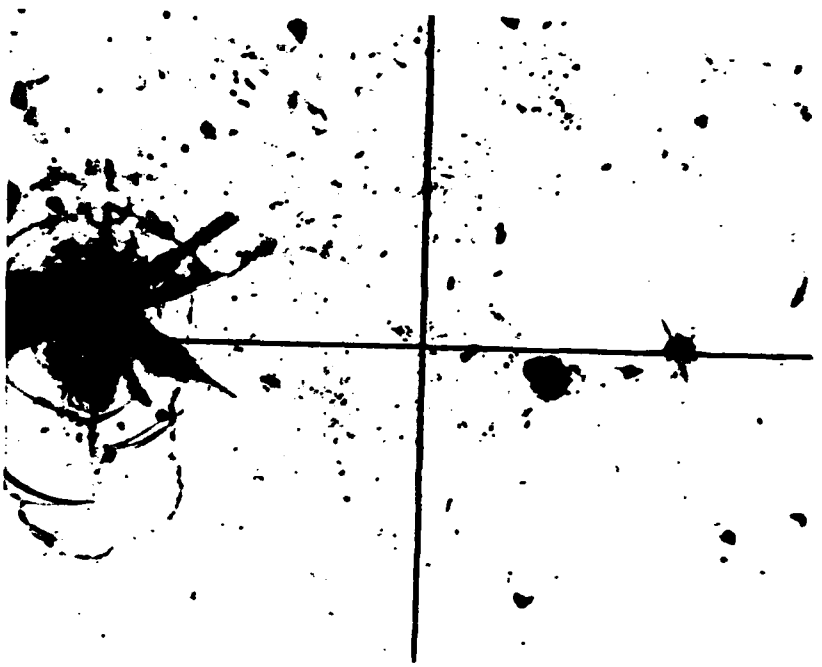

Figure 20. Comparison of Single Shot to 12 Shot Damage on Glass IOL (Both damage areas lie on horizontal cross hair. Other dark areas are dirt particles). Magnification = 42.5x.

the limit where multiple shots on the IOL would not cause total failure.

Total failure is presented in Figure 22 which shows the effects of three laser shots of 9.7mJ ($2.36 \times 10^{12} W/cm^2$) pulse energy each. On the second shot the IOL fractured into three pieces with the lower right section knocked out of the IOL frame on the following pulse. Note that a plastic IOL absorbing 10 shots of higher energy (10.89mJ), sustained relatively minor localized damage as shown in Figure 23.

Figure 21. Multishot Damage to Glass IOL
Magnification = 4.25x

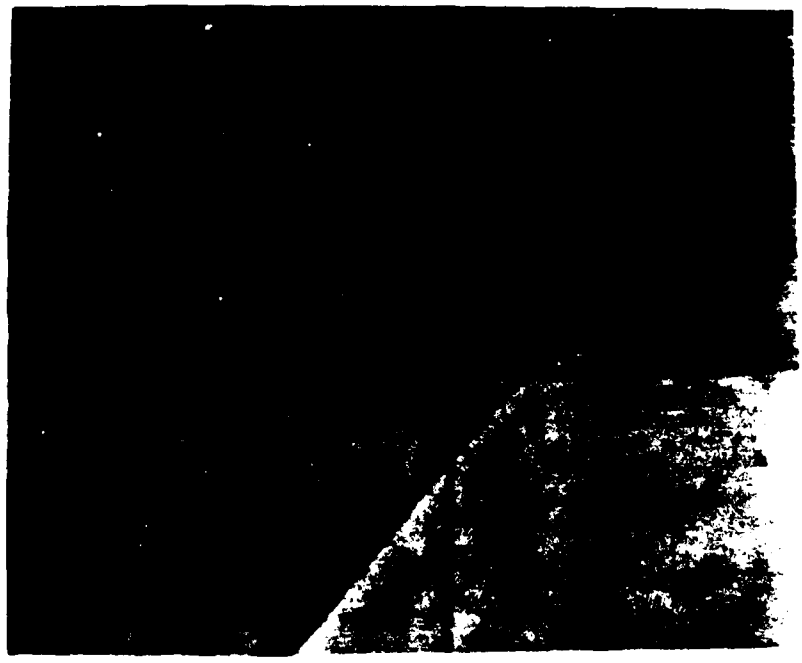

Figure 22. Total Failure of Glass IOL
Magnification = 4.25x

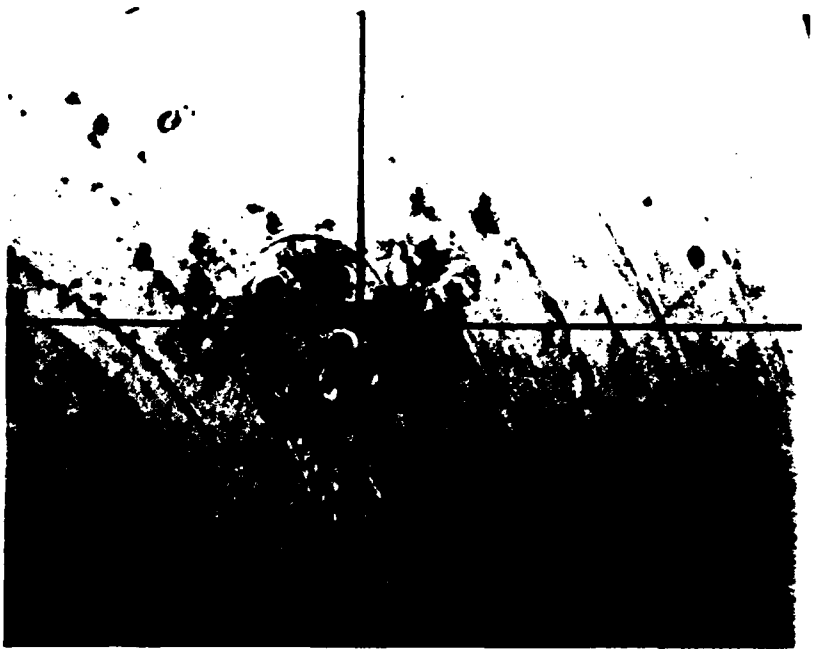

Figure 23. Multishot Damage to Plastic IOL
Magnification = 42.5x

An investigation of the effects of the beam on the opaque plastic frame of the glass IOL revealed its susceptibility to damage. The experiment, conducted only with relatively modest 5.67mJ ($1.38 \times 10^{12} W/cm^2$) pulses, is depicted in Figure 24. Figure 24(a) shows damage sustained by the lens frame after 10 shots to be extensive but not so extensive as to split the frame in two. Figure 24(b) shows the fracture of the plastic mounting clip after five shots of the same energy as used in Figure 24(a).

The second series of experiments on the glass IOL consisted of focusing the beam through the IOL on a fixed target where the IOL and target are immersed in tap water

a.

b.

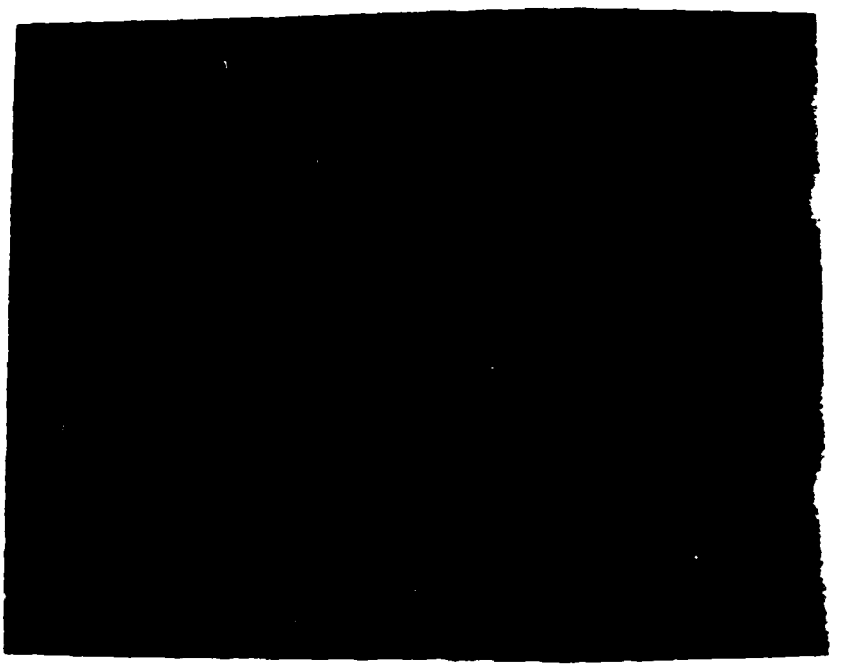

Figure 24. Damage to Glass IOL Components (Magnification = 4.25x). a) Frame: Large black area in center indicates damage to frame. The thick irregular line in the lower right corner

Figure 24 (Cont.). indicates where a small section of the IOL has broken off; b) Mounting Clip: Ragged edge in lower right quadrant resulted from breaking the mounting clip with laser pulses.

in the large, specialized test cell. The initial target-IOL distance was 1.59mm and the IOL was moved toward the target in increments of 317.5μm, equivalent to a ½ rotation of the IOL-mount-adjustment screw. At each interval, a single shot was fired, after which, if no damage was detected through the use of the binoculars, ten more shots were fired at a 1Hz rate. If no detectable damage occured at this point, a final round of ten shots was fired at 1Hz, the IOL inspected for damage, and the process repeated at the next distance interval.

The Nd-YAG beam was focused on the target in a manner simulating that of the ophthalmologist's use of the system to focus the beam in the eye. First the focusing lens was moved along the optical axis until the He-Ne beam formed the smallest, brightest spot on the target as viewed through the IOL. The pulse energy was then set at 10.89mJ ($2.65 \times 10^{12} W/cm^2$). Next, the Nd-YAG focus was verified by observing the plasma formation on the surface of the plastic target. The plasma remained attached to the target, extending only approximately 0.25mm upstream from the target. Occasionally, an isolated plasma formed in the water between the lens and the target and seemed to be initiated by the absorption of plastic particles ejected from the plastic on the previous strike.

Under these conditions the experimentation showed no damage to either glass or plastic implants until they were in contact with the target. At that time, one shot produced no damage observable with the binoculars but three additional shots fractured the lens and knocked the pieces from the frame.

Irradiation of the Eye

Two serious problems interfered with the acquisition of meaningful results from irradiation of pig and human eyes.

First, the location of the focusing optics forced the binoculars to be positioned such that the angle with which the eye was viewed was too large. The view of the capsule and vitreous was blocked by the iris.

Second, due to the close proximity of the focusing lens to the eye, splattered ocular tissue collected on the lens.

VII. Discussion

The relatively wide range of topics presented thus far, both theoretical and experimental, will be tied together in this chapter. The drawbacks and limitations of the experimental equipment design, and the experimental results will be discussed with their relationships to the theory developed in Chapters II-IV. Finally a theoretical analysis on the modification of the beam parameters to optimize the system based on the work in all preceding chapters will also be discussed.

System Drawbacks

The creation and accurate study of spark plasmas inherently requires a high degree of optical quality in the components, and an optimization of optical and mechanical design. When combined with the precision and reliability needed by the surgeon, the optimization requirements are even greater. Although attempts were constantly made during the design and construction phases to provide this optimization, the design failed in several respects.

First, the effects of primary spherical aberration were not minimized. Because the first focusing lens used, the achromat doublet (which was almost perfectly corrected for spherical aberration at 1.06μm), did not withstand the laser pulses aimed through it, the plano-convex lens system was used. Recall that this particualr system yielded a 4.9λ aberration function value. It is also felt that the beam

expander used may have contributed slightly to the system aberration although no calculations were performed.

Second, the use of a rotating slide beam attenuator created alignment problems at high angles (30°-50°) through the effects of refraction. The shift in the beam was minescule at the attenuator itself but the error was rapidly amplified with propagation through the articulated arm--which requires that the beam be perfectly centered at each elbow mirror. This problem caused no inaccuracies in the results, however, because the focusing optics were aligned each time the attenuator slide was rotated. At most, the alignment problem created nothing more than an inconvenience.

Third, a serious drawback was set by the limit on the pulse energy available. Ideally, the preferred pulse energy range would be from 5mJ to 100mJ in which it is felt lies the value where plasma formation on 100% of the laser shots would easily be attained in the BSS, vitreous, and distilled water. In that way, a more accurate picture of the breakdown characteristics of these solutions would be determined. The basic aspect of this problem, low energy out of the resonator, was aggravated by large losses from the beam attenuator surface reflection, copper mirror oxidation and beam expander absorption and reflection, and was measured to be 71.6%.

Fourth, the physical design prevented the slitlamp

binoculars from being used to view straight into the back of the eye.

For the current project, the effects of tissue splatter on the focusing optics already prevented experimentation on eyes so the problem with the binoculars was not a serious one. For future projects using the system, however, the design should be altered to allow viewing down the optical axis into the eye.

Discussion of Experimental Results

By extending the explosive threshold theory of gases and solids, described in Chapter III, to liquids, one would expect to observe in the current system, the inability to produce an arbitrarily small spark plasma on 100% of the laser shots. The reason for this is that the use of a relatively long pulsewidth and a wavelength in the near infrared, forces the dominant ionization mechanism to be cascade ionization. And, indeed, the explosive threshold was observed. At the minimum pulse energy which assured a 100% probability of plasma formation in tap water, plasma lengths of up to 2mm--more than 180 Rayleigh ranges--were detected.

The difference in the threshold level between tap water and distilled water supports the theory of absorbing particulates supplying the priming electrons for cascade ionization. Here, of course, one assumes a greater concentration of impurities in tap water than in distilled water. This theory then implies that the vitreous also has a

relatively low concentration of absorbing particulates due to the similarity of its breakdown characteristics with distilled water. This implication runs counter to intuition when one considers that the vitreous is not a true fluid but rather a hydrated gel composed of a network of microscopic collagen filaments (Ref 10:94, 96). Apparently, then, these organic particles do not have a sufficient absorption characteristic to produce a large number of priming electrons under the influence of the laser beam.

Regardless of the mechanisms involved with the plasma formation in the vitreous, the experimentation demonstrated that a BSS and distilled water both serve as adequate models for simulating plasma formation in the vitreous. The observed breakdown characteristics of the three fluids were essentially equivalent to the degree of accuracy of the measurements. In addition, it was demonstrated that for a system of similar beam parameters, pulse energies greater than 10.25mJ are needed to insure a 100% probability of plasma formation.

Even at power density levels less than that needed to insure a 100% probability of plasma formation, it takes only two to three shots focused on a glass IOL to shatter it. For an implant mounted in the anterior chamber where a finite space exists between the IOL and the opacified capsule, and assuming a skillfull operator of the laser, the capsule should be easily opened with no damage to the lens. However, for an IOL mounted in the posterior chamber

where the capsule is in contact with the implant, the procedure runs a high risk of shattering the implant.

Investigation of Alternate Beam Parameters

As stated throughout this paper, the optimal laser system for opening opacified tissue in the eye is one which allows the surgeon accurate placement of the spark plasma while depositing a minimal intensity on healthy segments of the eye.

Along these lines, then, the design criteria include a) utilizing a wavelength which is at the minimum of the absorption curves for the segments of the eye upstream of the desired plasma location. This insures minimizing the possibility of damage while maximizing the power transmission to the focus; b) choosing the proper values of wavelength and pulsewidth so as to eliminate the explosive threshold; and c) maximizing the entering cone angle of the beam for system perfectly corrected for primary spherical aberration.

Table 1 on page 15 is used when analyzing criterion (a). The values under the "vitreous" category indicate the percentage of a beam incident on the cornea which reaches the vitreous for various wavelengths. The values under the "direct" column indicate that wavelengths between 600 and 1100nm maximize direct transmission to the vitreous; values in the "total" column indicate that wavelengths between 500 and 900nm minimize the combined absorption of the cornea, aqueous, and lens. The difference is due to the amount of

scattered radiation at each wavelength. Note also that these values may vary slightly when the human lens is replaced by an IOL.

Criterion (b) is much more difficult to analyze theoretically because it involves extending the results of optical breakdown in gases and solids to that of liquids. Making this extension, however, it appears that reducing the wavelength of the incident radiation while at the same time reducing the pulsewidth may partially or totally eliminate the explosive threshold. This occurs, it is felt, through reduction of the dominance of cascade ionization and enhancement of ionization through multiphoton absorption. This, in combination with a large input cone angle, may enable one to achieve a 100% probability of plasma formation per shot with an arbitrarily small plasma length. The possible drawbacks of this method are a higher pulse power requirement to exceed the higher threshold associated with multiphoton absorption ionization, and the increasing risk of photochemical damage with decreasing wavelength. A physical drawback lies in the increased cost and maintenance problems associated with producing picosecond pulses; the system investigated in this thesis was designed to avoid this problem.

VIII. Recommendations and Conclusions

The recommendations for future work fall into two categories, design changes and future experiments, and are based on the discussion of the previous chapter.

Design Changes

The first suggested modification involves increasing the distance between the optics and the target so that when actual eyes are irradiated there will be no splattered tissue material forming on the optics. The cone angle into the eye can be held constant while the distance is increased by compensating with a greater amount of beam expansion.

A second proposed modification concerns the inability to view down the optical axis at the targets. A remedy for this problem is to perform the beam expansion and final focusing in the beam's final vertical path into the slitlamp. A final flat mirror at the slitlamp, tilted at 45°, can direct the beam into the target. The mirror should be constructed of sapphire or fused silica, HR coated at 1.06 μm for 100% reflection, and polished on the rear surface so as to be transparent to the visible. With this design, depicted in Figure 25, the binoculars can be positioned behind the mirror and the targets viewed at normal incidence. Note that with this design the problem of tissue splatter now affects the mirror and not the focusing lens.

A third suggested modification concerns the purchase or construction of a beam attenuator which utilizes cross

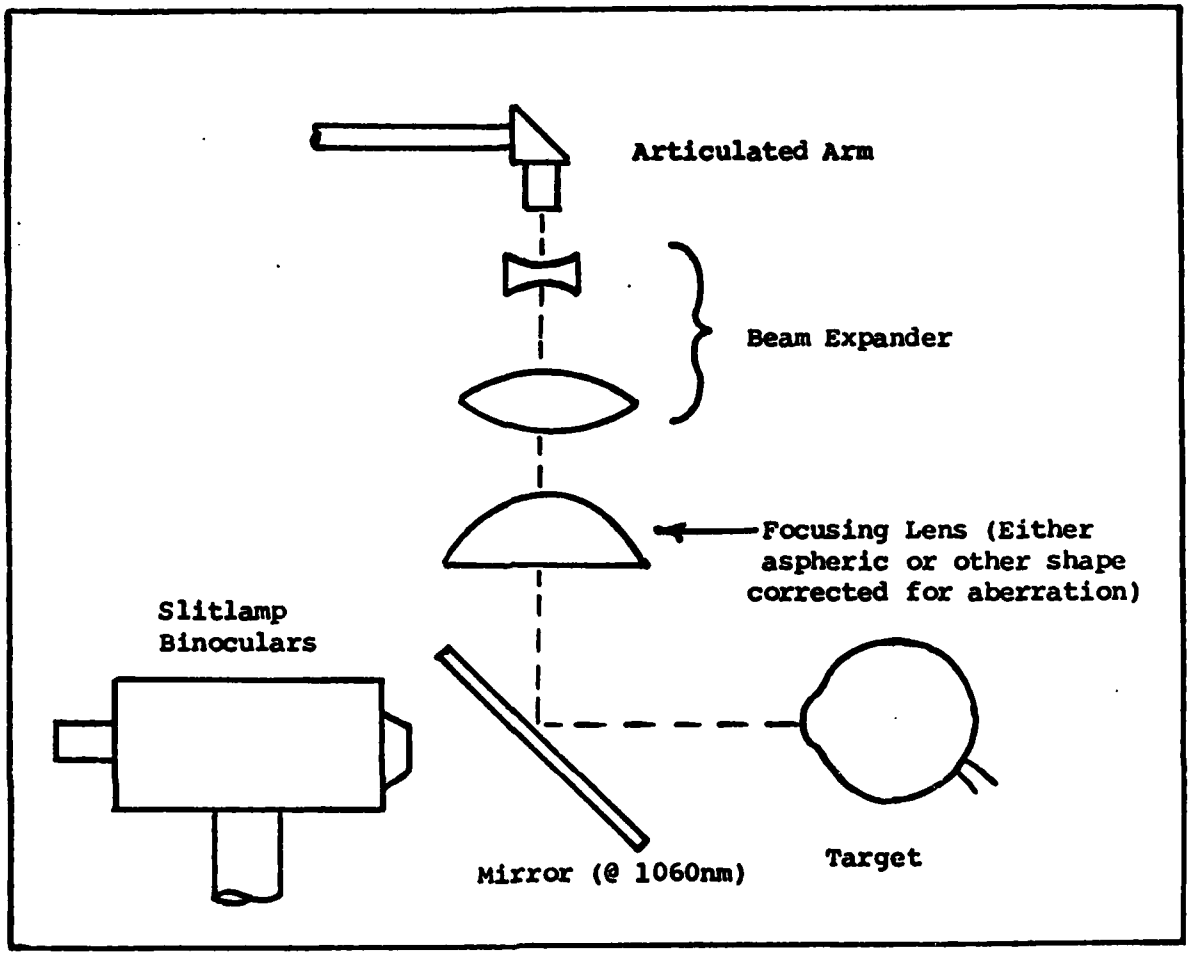

Figure 25. Alternate Design of Optical Interface

polarizers as opposed to a rotating slide. This design eliminates misalignment of the beam as it travels through the arm. Placing the attenuator beyond the output of the arm may also reduce misalignment problems.

A fourth modification involves the energy loss problem. If at all possible, a Nd-YAG or Nd-Glass laser with a higher peak energy in a TEM_{00} mode pulse should be used. Whether or not this is accomplished the system losses should be reduced by either repolishing the copper mirrors

and adding an anti-oxidation coating (if such a coating does exist), or replacing the copper mirrors with HR coated dielectric mirrors. The current beam expander should also be replaced by one containing AR coated optics.

Future Experimentation

The possibility of a system improvement through the use of shorter wavelengths and pulsewidths was discussed in Chapter VI. Because of the many parameters involved in plasma formation, combined with the complex biological nature of the human eye, the conjecture of Chapter VI must be accompanied by substantial experimentation. It may turn out that no substantial improvement is made or the amount of improvement is offset by design complexities and/or high cost. An interesting experiment might be to compare the use of a Q-switched doubled Nd-YAG laser operating at λ=530nm as a test of the use of a shorter wavelength. The use of a cavity dump mechanism yielding 1-10ns pulsewidths could also be studied to determine the effects of a pulse-width between that of a Q-switched system and that of a modelocked system.

The bulk of future testing should be performed on eyes as opposed to simulated systems to get a better indication of the effects of the cornea, aqueous, and either lens or lens implant on plasma formation in the vitreous. If the ocular experiments use a frequency doubled Nd-YAG system or other systems with a wavelength in the visible region, tests to detect the presence of photochemical damage to the

AD-A124 747 INVESTIGATION OF HIGH POWER PULSED NEODYMIUM-YAG LASERS 2/2
FOR CORRECTING OP.. (U) AIR FORCE INST OF TECH
WRIGHT-PATTERSON AFB OH SCHOOL OF ENGI.. J RIGGINS
UNCLASSIFIED JUN 82 AFIT/GEO/PH/82J-1 F/G 6/18 NL

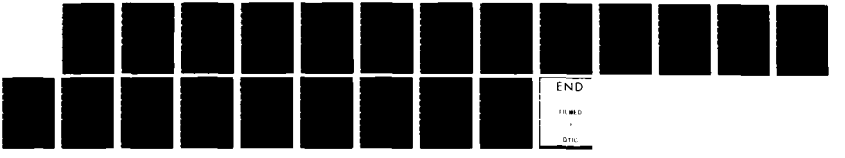

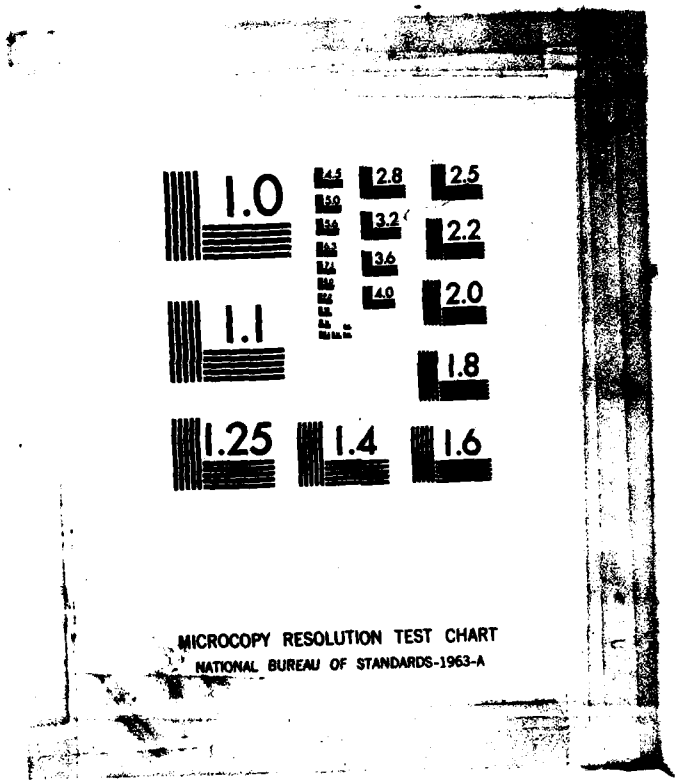
1.0
1.1
1.25
1.4
1.6
2.8
2.5
3.2
2.2
3.6
2.0
4.0
1.8
MICROCOPY RESOLUTION TEST CHART
NATIONAL BUREAU OF STANDARDS-1963-A

retina and human lens, if it is present, should also be conducted.

Finally, one totally different theory can be proposed which may also prove interesting to verify experimentally. Because of the opaqueness of the capsule, its absorption characteristics may give it a lower breakdown threshold than the surrounding vitreous and aqueous humor, and the IOL. If this is true, then it is reasonable to assume that a wavelength/pulsewidth combination exists such that the focused spot has a power density above threshold in the membrane but below threshold in the surrounding fluids and IOL. Thus, by focusing on the capsule instead of behind it (toward the retina), it could be ruptured with little risk of damage elsewhere in the eye.

Conclusions

A Q-switched Nd-YAG laser of pulsewidth 27ns was used to investigate the rupturing of ocular opacities through the initiation of optical breakdown and creation of a shock wave.

The laser, coupled to an ophthalmic slitlamp by an articulated arm, had maximum pulse energy of 10.89mJ at the output of the system, and a focused spot diameter of 4.4μm in air. Combined with a 27ns pulsewidth, the peak energy density at the focus in air was $2.89 \times 10^{12} W/cm^2$. The laser was fired mostly onto glass IOL's suspended in water to simulate the IOL being implanted in the eye.

The use of a Q-switched Nd-YAG laser system to open opacities in the eye is a feasible system only with the following restrictions: a) it cannot be used to open vitreous strands which may be located anywhere in the vitreous; b) restrictions on the input cone angle of the beam limit focusing to a distance of only 4-6mm behind the posterior capsule when the human lens is in place; and c) the use of the Q-switched system to open the posterior capsule with a glass IOL in place is risky when the capsule is in contact with the IOL, but not when the IOL is 300μm or greater from the capsule and the IOL. If struck by two or three laser pulses of greater than 9mJ, the glass IOL fails by shattering and dropping from its frame.

Finally, ocular plasma formation studies would be best carried out with the use of eyes as the target. If this is not possible, however, a balanced salt solution (BSS) can be used to best simulate the breakdown characteristics of the vitreous.

Bibliography

1. Theodossiadis, G.P. "Mobile Argon Laser Beam in Aphakic Pupillary Block," Lasers in Medicine, edited by Hans K. Koelner. New York: John Wiley & Sons, 1980.

2. Praska, Douglas, J. Design and Adaptation of an Optical System for Slit Lamp Delivery of a CO_2 Laser Beam. MS Thesis. Wright-Patterson AFB, Ohio: Air Force Institute of Technology, December 1981.

3. Kirsch, Ralph E. "Intraocular Lenses - The Conservative Approach," Controversy in Ophthalmology, edited by Robert J. Brockhurst, et al. Philadelphia, London, and Toronto: W. B. Saunders Company, 1977.

4. Dorell, E.D. Surgery of the Eye. London: Blackwell Scientific Publications, 1978.

5. Aron-Rosa, D. et al. "Use of the Neodymium - YAG Laser to Open the Posterior Capsule after Lens Implant Surgery: A Preliminary Report," Journal of the American Intraocular Implant Society, 6 (4): 352-354 (October 1980).

6. Fankhauser, Franz, et al. "Clinical Studies on the Efficiency of High Power Laser Radiation Upon Some Structures of the Anterior Segment of the Eye," International Ophthalmology, 3 (3): 129-139 (1981)

7. van der Zypen, E., et al. "Changes in the Ultrastructure of the Iris after Irradiation with Intense Light," Advances in Ophthalmology, 39: 59-180 (1979).

8. Sliney, David and Myron Wolbarsht. Safety with Lasers and Other Optical Sources. New York: Plenum Press, 1980.

9. Barnes, Frank S. "Applications of Lasers to Biology and Medicine," Proceedings of the IEEE, 63 (9): 1269-1277 (September 1975).

10. Lerman, Sidney. Radiant Energy and the Eye. New York: Macmillan Publishing Co., Inc., 1980.

11. Boettner, E.A. and J.R. Wolter. Transmission of the Ocular Media. 6570 Aerospace Medical Research Laboratories, Wright-Patterson AFB, OH, Technical Documentary Report No. MRL-TDR-62-34 (May 1962).

12. Geeraets, Walter J. and Edward R. Berry. "Ocular Spectral Characteristics as Related to Hazards from Lasers and Other Light Sources," American Journal of Ophthalmology, 66 (1): 15-20 (July 1968).

13. Cleary, S.F. "Laser Pulses and the Generation of Acoustic Transients in Biological Material," Laser Applications in Medicine and Biology, Volume 3, edited by M. L. Wolbarsht. New York: Plenum Press, 1977.

14. Milam, David. "Can a Model Which Describes Gas Breakdown also Describe Laser Damage to the Bulk and Surfaces of Solid Dielectrics," Proceedings of a Symposium on Laser Induced Damage in Optical Materials, edited by Alexander J. Glass and Arthur H. Guenther, 350-355, July 13-15 1976.

15. Morgan, C. Grey. "Laser-Induced Breakdown of Gases," Reports on Progresses in Physics, 38: 621-655 (1975).

16. Boni, A.A., and D.A. Meskan. "Effect of Impurities on Laser-Induced Air Breakdown at 1.06 ," Optics Communications, 14 (1): 115-118 (May 1973).

17. Bloembergen, Nicolaas. "Laser-Induced Electric Breakdown in Solids," IEEE Journal of Quantum Electronics, QE-10 (3): 375-386 (March 1974).

18. Shkarofsky, I.P. "Review of Gas-Breakdown Phenomena Induced by High-Power Lasers-I," RCA Review, 35: 48-77 (March 1974).

19. Aaron, J.M., et al. "Aberration Effects in the Interaction of Focused Laser Beams with Matter," Journal of Physics D: Applied Physics, 7: 1907-17 (1974).

20. Raizer, Yu P. "Breakdown and Heating of Gases Under the Influence of a Laser Beam," Soviet Physics Uspekhi, 8 (5): 650-671 (March-April 1966).

21. Morrison, R.W. and C. Swail. "Some Characteristics of CO_2-Laser-Induced Multiple Spark Breakdown at Pressures up to 11 atm," Journal of Applied Physics, 46 (9): 3817-27 (September 1975).

22. Bettis, J.R., et al. "Spot Size and Pulse Duration Dependence of Laser-Induced Damage," Proceedings of a Symposium on Laser Induced Damage in Optical Materials, edited by Alexander J. Glass and Arthur H. Guenther, 338-341, July 13-15 1976.

23. Barnes, Peter A. and K.E. Rieckhoff. "Laser Induced Underwater Sparks," Applied Physics Letters, 13 (8): 282-284 (October 15 1968).

24. Bell, C.E. and J.A. Lanott. "Laser-Induced High-Pressure Shock Waves in Water," Applied Physics Letters, 10 (2): 46-48 (January 15 1967).

25. Weichel, H. and L.S. Pedrotti. "A Summary of Useful Laser Equations - An LIA Report," Electro-Optical Systems Design, 8: 22-36 (July 1976).

26. Duke-Elder, Stewart. The Practice of Refraction (Seventh Edition). St. Louis: The C. V. Mosby Company, 1963.

27. Landry, Murphy J. Large Laser Energy and Power Transmitted Through Optical Fibers. Issued by Sandia Laboratories, Albuquerque, New Mexico. Report No. SAND78-0602 (June 1978).

28. Yoshida, A. and T. Asakura. "A Simple Technique for Quickly Measuring the Spotsize of Gaussian Laser Beams," Optics and Laser Technology: 273-274 (December 1976).

29. Melles Griot. Optics Guide 2. Product Catalog, Irvine, California: Melles Griot, 1981.

30. Wolfe, William L. and George J. Zissis. The Infrared Handbook. Prepared by the Infrared Information and Analysis (IRIA) Center, Environmental Research Institute of Michigan, 1978.

31. Klein, Miles V. Optics. New York: John Wiley & Sons, 1970.

32. Gerrard, A and J.M. Burch. Introduction to Matrix Methods in Optics. London: John Wiley & Sons, 1975.

APPENDIX A

Derivation of Validity Conditions for Geometrical Beam Approximations*

For the system of Figure 10, the distance z_2' can be found as follows. Extend the system matrix to include the translation, i.e.

$$M=\begin{bmatrix}1 & z_2'\\ 0 & 1\end{bmatrix}\begin{bmatrix}A & B\\ C & D\end{bmatrix}=\begin{bmatrix}(A+Cz_2') & (B+Dz_2')\\ C & D\end{bmatrix} \qquad [A-1]$$

Then at z_2', the geometric ray vector is

$$\begin{bmatrix}Y_2\\ V_2\end{bmatrix}=M\begin{bmatrix}Y_1\\ V_1\end{bmatrix}=\frac{(A+Cz_2')Y_1+(B+Dz_2')V_1}{CY_1+DV_1} \qquad [A-2]$$

At the geometrics focus, $Y_2=0$, therefore

$$(A+Cz_2')Y_1+(B+Dz_2')V_1=0$$

$$z_2'=\frac{-(AY_1+BV_1)}{(CY_1+DV_1)} \qquad [A-3]$$

After the far field assumption is made, the following substitutions can be made. $V_1=v_1(1)=-\theta_1$ and $Y_1=w_1$. The minus sign preceding θ is due to the sign convention

*The notations and sign conventions used in this matrix optics analysis can be found in Reference 32.

adopted for V_1: for a converging beam, $V_1<0$. With these substitutions made,

$$z_2' = -\frac{-A(W_1/\theta_1)+B}{-C(W_1/\theta_1)+D} = \frac{A(W_1/\theta_1)-B}{-C(W_1/\theta_1)+D} \qquad [A-4]$$

For the Gaussian beam, the input to the system is a distance $-z_1$ from the waist of the input beam and the output plane is at a distance $-z_2$ from the waist of the output beam. From the ABCD law of Gaussian optics,

$$-z_2+jz_{R2} = \frac{A(-z_1+jz_{R1})+B}{C(-z_1+jz_{R1})+D} \qquad [A-5]$$

which is Equation 6 on page 42.

By solving for the real part, $-z_2$, Equation A-6 is obtained

$$-z_2 = \frac{-(Az_1-B)(-Cz_1+D)+z_{R1}^2AC}{(-Cz_1+D)^2+z_{R1}^2C^2} \qquad [A-6]$$

or

$$z_2 = \frac{(Az_1-B)(-Cz_1+D)-z_{R1}^2AC}{(-Cz_1+D)(-Cz_1+D)+z_{R1}^2C^2} \qquad [A-7]$$

By definition (Ref 25:32),

$$w_1 = w_0\left(1+\left(\frac{\lambda z}{\pi w_0^2}\right)^2\right)^{\frac{1}{2}} \qquad \text{[A-8]}$$

from which the value for z, given in Equation 8, is found.

With the far field approximation, $W_{01}^2 << W_1^2$ and $z_{R1}^2 << z_1^2$ where W_{01} is the spotsize of the input beam waist,

$$\begin{aligned} z_2 &= \frac{-AC(z_1^2+z_{R1}^2)+BCz_1-BD+ADz_1}{C^2(z_1^2+z_{R1}^2)-2CDz_1+D^2} \\ &\approx \frac{-ACz_1^2+BCz_1-BD+ADz_1}{C^2z_1^2-2CDz_1+D^2} \\ &= \frac{(Az_1-B)(-Cz_1+D)}{(-Cz_1+D)^2} \\ &= \frac{Az_1-B}{(-Cz_1+D)} \\ &\approx \frac{A(w_1/\theta_1)-B}{-C(w_1/\theta_1)+D} \end{aligned} \qquad \text{[A-9]}$$

The equality of the results of Equations [A-4] and [A-9] demonstrates the validity of the far field assumption.

APPENDIX B

Derivation of the Retinal Spotsize when Focusing Behind the Posterior Capsule

The use of geometrical optics with the far field assumption described in Chapter IV and Appendix A will again be used to find an approximate value for the retinal spotsize when focusing at a distance d behind the posterior capsule. The value will be based on the geometrical cone angle in the vitreous behind the focus.

The matrix M_2 (where lengths are give in mm) on page 44, yields the following system of equations

$$Y_2=(0.7275-0.04655d)Y_0+(5.944+0.6531d)V_0 \quad [B-1]$$

$$V_2=-0.06191Y_0+0.8687V_0$$

Since the ray travels in a homogeneous medium from the focus to the retina, the cone angles are identical for all the values of d used. Picking d=0, which is at the focus,

$$Y_2=0=0.7275Y_0+5.944V_0 \quad [B-2]$$

or $$Y_0=-8.17V_0$$

and substituting into Equation [B-1] gives

$$V_2 = 1.3745V_0 = 1.3745(v_0/1) = 1.3745v_0 \qquad [B-3]$$

where the maximum values of v_0 for a given d were graphed in Figure 12 on page 46.

Because the capsule-retina distance is 14.35mm, the retinal spotsize can be given by

$$\begin{aligned} w &= (14.35-d)\tan|v_2| \\ &= (14.35-d)\tan[|v_2|/1.33] \\ &= (14.35-d)\tan(1.033|v_0|) \end{aligned} \qquad [B-4]$$

where the index of the vitreous = 1.33 is used.

Using the values of v_0 from Figure 12 and Equation [B-4] the graph of Figure 13 results. Note that although values of d from 0 to 14.35mm are graphed, the far field assumption begins to break down after only 5 or 6mm when the maximum, input, full cone angle is forced below 10° due to the effects of the iris. The breakdown of the assumption is of no consequence, however, because focusing closer and closer to the retina also forces a large increase in focused spotsize and Rayleigh range, and would, therefore, not be attempted.

APPENDIX C

Test Cell Construction

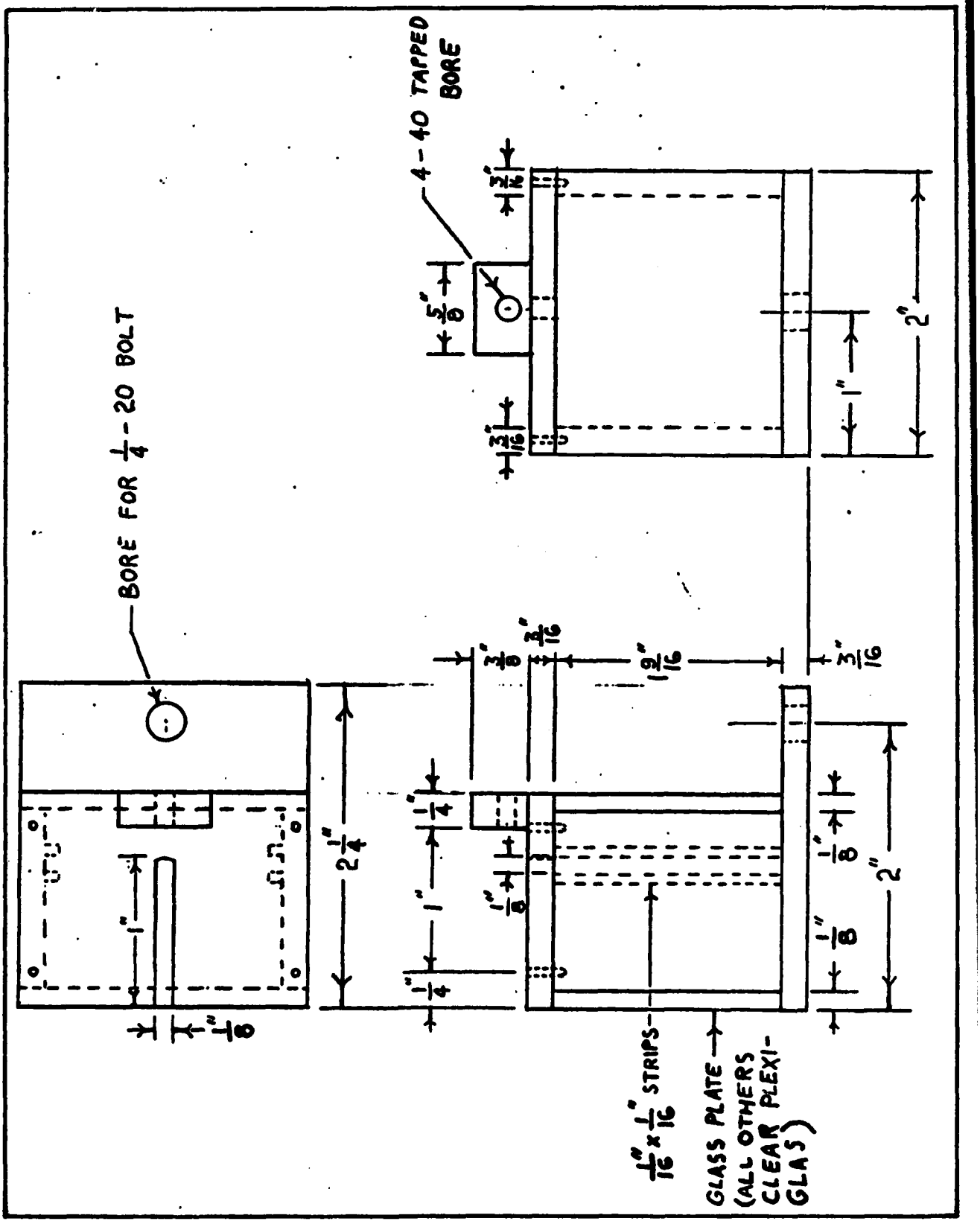

APPENDIX D

Aberration Function Calculation

Because the two plano-convex focusing lenses were in contact, although not across an entire face, it was assumed that the spherical aberration function, Φ would equal the sum of the two individual functions, ϕ_1 and ϕ_2 where ϕ_1 corresponds to the lens whose flat surface faces the incident beam. The ϕ values, given by (Ref 31:147), are

$$\Phi_i = G_i (D/2)^4 \qquad [D-1]$$

where D is the diameter of the beam incident on the lens--of focal length f and index of refraction n--and

$$G_i = \frac{1}{32 f^3 n (n-1)} \left(\frac{n+2}{n-1}\right) q_i^2 + 4(n+1)(p_i q_i) + (3n+2)(n-1)(p_i^2) + \frac{n^3}{n-1} \qquad [D-2]$$

The values of p_i and q_i are based on the shape of the lens and are given in this case by $q_1=-1$, $q_2=1$ and $p_1=p_2=-1$. Substituting these values into Equation [D-2] with f=8cm, and n=1.507, and summing G_1 and G_2 yields

$$G_1+G_2 = 1/(32 f^3 (0.764))[13.834+0+6.612+6.75]$$
$$= 2.173 \times 10^3 \qquad [D-3]$$

Therefore, for D=1.4cm and $\lambda=1.06\times10^{-4}$cm

$$\phi=(G_1+G_2)(D/2)^4$$

$$=(2.173\times10^{3})(2.4\times10^{-9})$$

$$=5.214\times10^{-6}$$

$$=4.9\lambda. \qquad [D-4]$$

APPENDIX E

Focused Spotsize Measurement

Figure E-1 below illustrates the procedure used to determine the focused spotsize.

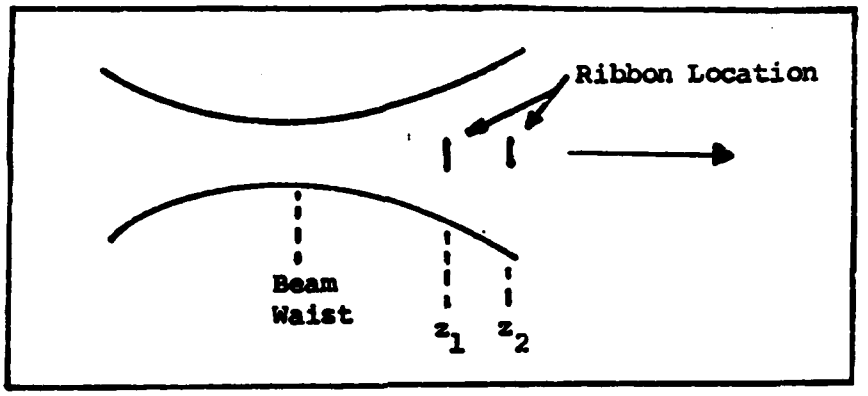

Figure E-1. Focused Spotsize Measurement

A ribbon of width 2a=0.86mm±.01mm was placed first at point z_1, well into the far field (approximately 5mm from the focus). The minimum charge reading made when the ribbon was located in the beam center was $C_{m1}=1.45\times10^{-9}\pm 3.13\times10^{-11}$Coul. The charge reading is a direct reading from the EG&G 580 radiometer and is proportional to the peak power. The constant factors needed to convert to power will cancel in the equations to follow.

The charge read at z_1 with no ribbon in place was $C_1=1.90\times10^{-9}\pm3.19\times10^{-11}$C.

Similarly, at z_2, the values measured were $C_{m2}=0.75\times10^{-9}C\pm 3.20\times10^{-11}C$ and $C_2=1.90\times10^{-9}C\pm3.19\times10^{-11}C$. The value of $|z_2-z_1|=6.35mm\pm.03mm$. The calculation of the focused spot-size proceeds as follows:

$$\frac{POWER_{max}}{POWER_{incident}}=\frac{C_m}{C_i}=erfc(x_i)=1-erf(x_i) \qquad [E-1]$$

where erf is the error function, whose values are found in most books of mathematical tables. Thus,

$$erf(x_i)=1-(C_m/C_i) \qquad [E-2]$$

and

$$x_i=a\sqrt{2}/w_i \rightarrow w_i=a\sqrt{2}/x_i \qquad [E-3]$$

With the spotsizes (w_i) at z_1 and z_2 found, the far field divergence,

$$\theta=\tan^{-1}((w_2-w_1)/(z_2-z_1))=\lambda/(\pi w_0) \qquad [E-4]$$

or

$$w_0=\lambda/(\pi\theta) \qquad [E-5]$$

The results of these calculations when numerical values have been applied, are given in Chapter V. The remainder of this Appendix will present the associated error analysis, conducted by propagating the standard deviations (S) of all measurements through the calculations.

$$S^2_{erf_i} = \left(\frac{\partial erf}{\partial C_{mi}}\right)^2 S^2_{Cmi} + \left(\frac{\partial erf}{\partial C_i}\right)^2 S^2_{Ci}$$

$$= (1/C_i^2) S^2_{Cmi} + (C^2_{mi}/C^4_i) S^2_{Ci} \qquad [E-6]$$

Therefore,

$$S^2_{erf_1} = 4.4606 \times 10^{-4} \text{ and } S^2_{erf_2} = 3.2581 \times 10^{-4}$$

A linear interpolation was used on the table of erf(x) to find x_i from a given $erf(x_i)$. Because the correlation coefficient associated with five points near the points of interest in the table is 0.999997, the linear interpolation induces little error. It is therefore assumed that the relative error

$$\frac{S^2_{erf}}{erf^2(x_i)} = \frac{S^2_{xi}}{x_i^2}$$

or

$$S^2_{xi} = \frac{S^2_{erf} x_i^2}{erf^2(x_i)} \qquad [E-7]$$

Then, using Equation [E-3]

$$S_{wi}^2=(\sqrt{2}/x_i)^2S_a^2+(\sqrt{2}a/x_i^2)^2S_{xi}^2 \qquad [E-8]$$

giving $S_{wi}^2=1.3812\times10^{-3}mm^2$ and $S_{w2}^2=4.846\times10^{-2}mm^2$. Now, define $Q=w_2-w_1$ so that $\theta=\tan^{-1}(Q/(z_2-z_1))=\tan^{-1}(Q/\Delta z)$. Then

$$S_Q^2=S_{w2}^2-S_{w1}^2 \qquad [E-9]$$

and

$$S_\theta^2=\left(\frac{\partial\theta}{2Q}\right)^2S_Q^2+\left(\frac{\partial\theta}{\partial\Delta z}\right)^2S_{\Delta z}^2$$

$$=\left(\frac{\Delta z}{\Delta z^2+Q^2}\right)^2S_Q+\left(\frac{Q}{\Delta z^2+Q^2}\right)^2S_{\Delta z}^2 \qquad [E-10]$$

with numerical values of

$$S_Q^2=4.9843\times10^{-2}mm^2$$

$$S_\theta^2=1.179\times10^{-3}rad^2$$

Finally using

$$S_{w0}^2=[(1/(\pi\theta))^2S_\lambda^2+(-\lambda/(\pi\theta^2))^2S_\theta^2]$$

$$=2.3793\times10^{-7}mm^2$$

giving the desired result,

$$S_{w0}=0.488\mu m$$

Vita

James Riggins was born on 19 December 1958 in Wilmington, Delaware. Upon graduating from Brandywine High School in 1976, he entered the United States Air Force Academy where he received a Bachelor of Science degree in Electrical Engineering. He received his commission in December of 1980 from the Academy and entered the Air Force Institute of Technology at Wright-Patterson AFB, Ohio shortly thereafter.

Permanent Address: 1450 Forsythia Avenue
Wilmington, DE 19810

UNCLASSIFIED

SECURITY CLASSIFICATION OF THIS PAGE (When Data Entered)

REPORT DOCUMENTATION PAGE		READ INSTRUCTIONS BEFORE COMPLETING FORM
1. REPORT NUMBER AFIT/GEO/PH/82J-1	2. GOVT ACCESSION NO. AD-A124747	3. RECIPIENT'S CATALOG NUMBER
4. TITLE (and Subtitle) INVESTIGATION OF HIGH POWER, PULSED, NEODYMIUM-YAG LASERS FOR CORRECTING OPACITIES OF THE HUMAN EYE		5. TYPE OF REPORT & PERIOD COVERED MS Thesis 6. PERFORMING ORG. REPORT NUMBER
7. AUTHOR(s) JAMES RIGGINS 2Lt USAF		8. CONTRACT OR GRANT NUMBER(s)
9. PERFORMING ORGANIZATION NAME AND ADDRESS AF Institute of Technology (AFIT-EN) Wright-Patterson AFB OH 45433		10. PROGRAM ELEMENT, PROJECT, TASK AREA & WORK UNIT NUMBERS
11. CONTROLLING OFFICE NAME AND ADDRESS		12. REPORT DATE June 1982 13. NUMBER OF PAGES 113
14. MONITORING AGENCY NAME & ADDRESS(if different from Controlling Office)		15. SECURITY CLASS. (of this report) UNCLASSIFIED 15a. DECLASSIFICATION/DOWNGRADING SCHEDULE

16. DISTRIBUTION STATEMENT (of this Report)

Approved for Public Release; Distribution Unlimited.

17. DISTRIBUTION STATEMENT (of the abstract entered in Block 20, if different from Report)

18. SUPPLEMENTARY NOTES

Approved for public release: IAW AFR 190-17.

LYNN E. WOLAVER
Dean for Research and Professional Development
Air Force Institute of Technology (ATC)
Wright-Patterson AFB OH 45433

4 JA

19. KEY WORDS (Continue on reverse side if necessary and identify by block number)

Posterior Capsule Nd-YAG Laser

Ophthalmic Slitlamp

Optical Breakdown

20. ABSTRACT (Continue on reverse side if necessary and identify by block number)

A Q-switched Nd-YAG laser system with a 27ns pulsewidth and focused spotsize diameter in air of 4.4μm is used in a series of experiments related to opening ocular opacifications. The maximum pulse energy is 10.89mJ yielding a peak focused intensity of $2.65 \times 10^{12} W/cm^2$.

Results of experiments designed to simulate opening an opacified posterior capsule after cataract surgery and glass IOL

DD FORM 1 JAN 73 1473 EDITION OF 1 NOV 65 IS OBSOLETE

UNCLASSIFIED

SECURITY CLASSIFICATION OF THIS PAGE (When Data Entered)

Block 20: ABSTRACT: (Cont'd)

implantation indicate an occurrence of IOL shatter only when the IOL is in contact with the capsule.

Additional experiments on the optical breakdown characteristics of several fluids indicate balanced salt solution most closely models the breakdown characteristics of human vitreous.

A theoretical feasibility analysis of using the laser system to rupture vitreous strands concludes that only rupturing strands no farther than 4-6mm from the posterior capsule in an undilated eye can be safely attempted.

Finally, a general theoretical analysis on the effects of altering beam parameters--wavelength, pulsewidth, spotsize--reveals possible benefits of utilizing short wavelength (down to 500nm)/short pulsewidth systems (picosecond).

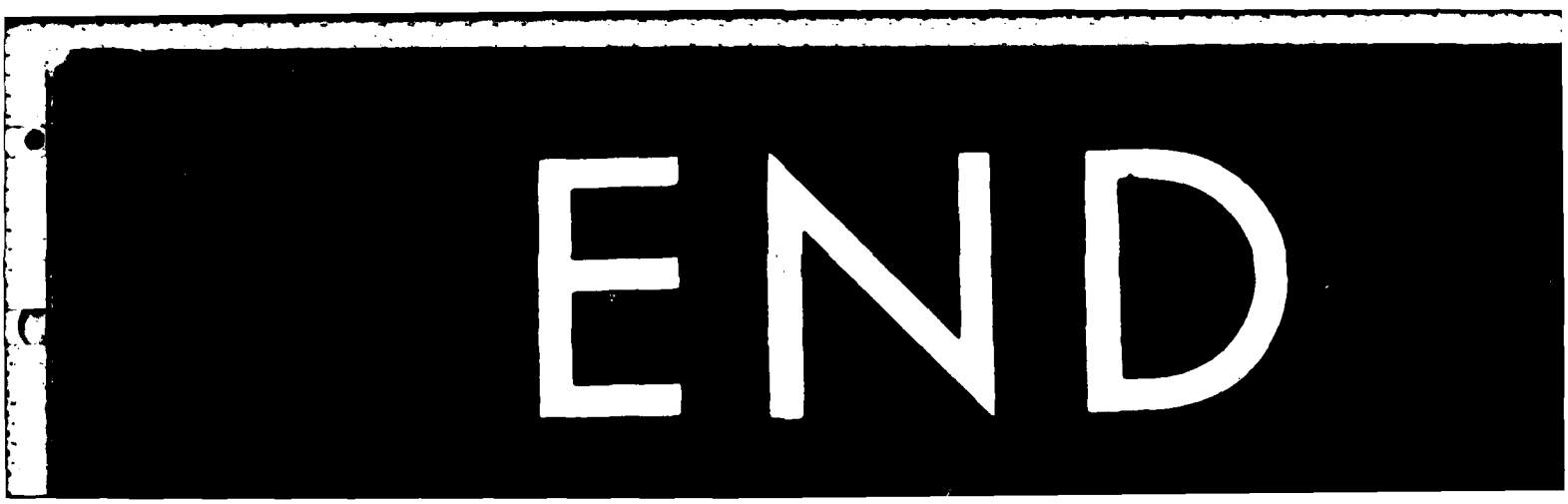
END